Materials & Design 258 (2025) 114684

Contents lists available at ScienceDirect

Materials & Design

journal homepage: www.elsevier.com/locate/matdes

In-Situ microstructure characterization and micromechanical modelling of damage initiation and propagation in DP1000 dual phase steel

Asim Alsharif [a,b,*], Syed Quadir Moinuddin [c,**], R. Dowding [a], C. Pinna [a,***]

[a] Department of Mechanical Engineering, The University of Sheffield, Mappin Street, S13JD Sheffield, UK
[b] Department of Mechanical Engineering, College of Engineering at Yanbu, Yanbu Al-Bahr 41911, Saudi Arabia
[c] Department of Mechanical Engineering, College of Engineering, King Faisal University, Al-Ahsa, 31982, Saudi Arabia

ARTICLE INFO

Keywords:
DP 1000 Steel
In-situ Tensile Test with DIC
Bending test
SEM
Damage Mechanism
FEM Simulation

ABSTRACT

Dual Phase (DP) steels are widely used in the automotive industry due to their excellent strength-ductility balance. Advancing next-generation steels requires a deeper understanding of deformation and damage mechanisms at the microstructural level. The present study investigates damage initiation and propagation in DP1000 steel through in-situ tensile and bending tests inside a scanning electron microscope (SEM), combined with digital image correlation (DIC) for strain mapping. Results show that plastic deformation localizes in ferrite, while damage initiates at ferrite-martensite interfaces and propagates within martensite islands during early plastic deformation. Finite element (FE) simulations reveal a correlation between local stress and martensite damage initiation, whereas ferrite damage events remain limited. Bending tests further highlight crack formation along strain localization paths in ferrite. These findings provide valuable insights for predictive multi-scale modelling of DP steels. Finally, the Gurson-Tvergaard-Needleman (GTN) damage modelling approach was adopted to predict the load–displacement curve of the tensile sample by calibrating damage parameters.

1. Introduction

The increasing demand for fuel efficiency and crashworthiness in the automotive industry has accelerated the development of advanced high-strength steels (AHSS). Dual-Phase (DP) steels are among the most widely employed AHSS due to their excellent combination of high strength and ductility, arising from a microstructure of soft ferrite reinforced by hard martensite islands [1–3]. First-generation AHSS, including DP600 and DP780, offered a favourable balance of strength and formability for early automotive lightweighting applications. The second generation of AHSS, which includes high-manganese austenitic steels such as TWIP and L-IP steels, provides superior formability and energy absorption. These steels achieve enhanced mechanical performance through alloying strategies that stabilize austenite, primarily via manganese and carbon additions [3,4]. However, their application is limited by high alloying costs, complex processing, and susceptibility to delayed cracking. Third-generation AHSS, exemplified by DP980 and DP1000, achieve an optimized strength-ductility combination through precise alloy design and thermomechanical processing, making them ideal for advanced structural components [7,8].

Despite their growing industrial relevance, understanding damage initiation and fracture behavior in DP steels remains complex due to factors such as stress–strain heterogeneity, martensite morphology, and ferrite–martensite interfacial interactions. A transformative development in addressing these complexities was the adoption of micro-scale Digital Image Correlation (micro-DIC), first demonstrated by Kang et al. [9] for surface strain mapping in aluminium alloys using SEM-based topographical correlation. This method was subsequently extended to DP steels [10,11], enabling quantitative strain measurements at the microstructural scale. Studies employing micro-DIC on DP600–DP1000 grades [12–16] revealed that plastic deformation localizes within ferrite, concentrating stress in adjacent martensite regions and facilitating micro-crack initiation. Notably, in DP600, localized strain accumulation around ferrite–martensite interfaces was successfully visualized at high spatial resolution [10,11].

Early investigations into damage initiation in DP steels revealed that void nucleation predominantly occurs at ferrite–martensite interfaces, with martensite cracking observed at relatively low global strains (~13

* Corresponding author at: Department of Mechanical Engineering, The University of Sheffield, Mappin Street, S13JD Sheffield, UK.
** Corresponding author at: Department of Mechanical Engineering, College of Engineering, King Faisal University, Al-Ahsa, 31982, Saudi Arabia
*** Corresponding author at: Department of Mechanical Engineering, The University of Sheffield, Mappin Street, S13JD Sheffield, UK.
E-mail addresses: aasharif@taibahu.edu.sa (A. Alsharif), smoinuddin@kfu.edu.sa (S.Q. Moinuddin), c.pinna@sheffield.ac.uk (C. Pinna).

https://doi.org/10.1016/j.matdes.2025.114684
Received 9 July 2025; Received in revised form 24 August 2025; Accepted 1 September 2025
Available online 2 September 2025

%) [17,18]. Avramovic-Cingara et al. [17] reported micro-crack formation in martensite at a local strain of ~ 0.029 in DP600, followed by void nucleation at the ferrite–martensite interface around 0.09 strain. Ghadbeigi et al. [18] further identified complex interactions involving interfacial decohesion, martensite cracking, and void coalescence. Extending this understanding to DP780, Saeidi et al. [19] emphasized, through SEM analysis, that damage frequently initiates at triple-phase junctions and within narrow ferrite regions bounded by martensite islands. As a fracture is typically preceded by localized plastic deformation, understanding how strain accumulates and evolves into damage is essential. These studies collectively underscore the critical role of microstructural topology, particularly ferrite bands embedded between martensite and aligned along the loading direction, in governing localized deformation and early-stage damage, especially under uniaxial loading. Further contributions [20,21] investigated band formation and fracture in ferrite using SEM and in-situ techniques. Time-resolved SEM-based tensile tests on DP800 [22] tracked void evolution from diffuse necking to final failure, revealing voids between ferrite and martensite as well as within ferrite grains. Alaie et al. [23] complemented these observations by developing a dislocation-based constitutive model for ferrite, integrating DIC data and simulations to quantify localized deformation. Their model showed higher strain accumulation in ferrite, strongly influenced by martensite island size and distribution. Complementing these experimental studies, Matsuno et al. [24] performed three-dimensional finite element analyses of representative volume elements to examine the effects of martensite morphology and banding on the tensile behavior of ferrite–martensite DP steels, demonstrating how phase distribution influences macroscopic mechanical properties. Ohata et al. [25] introduced a damage-based framework to evaluate ductile cracking in steel structures under large-scale cyclic loading, emphasizing the influence of microstructural inhomogeneity on fracture evolution. More recently, Gu and Kwon [26] combined nano- and bulk-scale digital image correlation with finite element simulations to determine damage model parameters, demonstrating the significant impact of microstructural features on damage initiation and propagation.

Alharbi et al. [27] focused on DP1000, employing SEM, DIC, and finite element (FE) modeling to explore martensite-initiated fracture. The first voids appeared at inclusions before testing, followed by voids at the ferrite–martensite interface at approximately 32 % strain, with final separation of martensite islands occurring at around 52 % strain. Ososkov et al. [11] analyzed strain partitioning in DP600, reporting ferrite strain variations from 30 % to 70 %, and identified void nucleation between adjacent martensite islands at local strains of about 0.4. Ghadbeigi et al. [18] conducted in-situ SEM tensile tests on DP1000, revealing martensite fracture and interfacial decohesion at local strain levels up to 120 %. Their follow-up work on DP600 [19] utilized novel gauge geometries, confirming sub-micron voids and crack paths linked to inclusions and ferrite grain decohesion. Alaie et al. [23] extended this by formulating a dislocation-based model capturing strain gradients within ferrite between martensite clusters, further supporting the role of localized deformation in early damage evolution. Despite these significant efforts, a comprehensive understanding of micro-scale damage mechanisms in higher-strength DP steels like DP1000, particularly under combined loading conditions, remains limited.

Building on the microstructural insights provided by in-situ experiments and DIC analyses, the modeling of ductile fracture in DP steels has increasingly relied on micromechanical approaches such as the Gurson–Tvergaard–Needleman (GTN) model. Originally developed by Gurson [28], the model describes void nucleation, growth, and coalescence as a function of hydrostatic stress and void volume fraction, offering a continuum-based framework for predicting ductile failure in porous media. Tvergaard's modifications [29–31] introduced fitting parameters (q_1, q_2, q_3) that capture the influence of material-specific behavior, particularly under shear localization and varying triaxiality conditions, thereby improving the model's agreement with finite element (FE) simulations.

Several researchers have tailored the GTN model to simulate damage in DP steels. Qin et al. [32] implemented GTN and cohesive zone models to simulate martensite cracking, emphasizing the influence of phase distribution on fracture progression. Similarly, Kim et al. [33] analyzed the effects of stress triaxiality and porosity on void growth, reinforcing the need for accurate parameter calibration in multiphase materials. Zhang et al. [34] advanced this field by developing a hybrid experimental–numerical framework that integrates GTN modeling with DIC measurements to characterize fracture under complex loading paths. Meanwhile, parameter identification has evolved through approaches such as response surface methodology [35] and direct experimental evaluation of critical void volume fractions [36]. Modifications proposed by Nahshon and Hutchinson [37] further expanded the GTN model to incorporate shear damage, making it more suitable for predicting failure under real-world automotive loading conditions.

Finite element simulations further complement experimental observations by capturing strain gradients and stress localization that may not be directly measurable. Modeling of DP steels consistently shows that strain partitions between hard martensite and soft ferrite, with morphological features such as the aspect ratio of martensite significantly influencing ductility, yield strength, and damage localization [38–40]. Additionally, the martensite volume fraction governs the trade-off between strength and formability, highlighting the critical role of microstructural design in optimizing the performance of DP steels. Despite these advancements, a comprehensive understanding of micro-scale damage mechanisms in high-strength grades like DP1000, particularly under complex loading conditions, remains incomplete, necessitating further integration of experimental data with predictive modelling. From the literature, it is evident that a deeper, experimentally validated understanding of strain localization and damage evolution in high-strength DP steels, particularly under different loading modes, is still lacking. The present study aims to bridge the gap between experimental observations and numerical Modeling in understanding damage initiation and evolution in high-strength dual-phase steels, specifically DP1000. The primary objective is to investigate strain localization and microstructural damage mechanisms through in-situ tensile and bending tests conducted inside an SEM. DIC is employed to map local strain fields at the microstructural scale, enabling correlation between deformation behavior and void/crack formation. FE simulations, calibrated using experimental data, are used to analyze stress distributions and validate micromechanical models. Furthermore, the study applies the GTN damage model to simulate void nucleation and growth, offering insight into failure progression under complex loading conditions. This integrated approach aims to improve the predictive accuracy of ductile fracture models by incorporating real-time experimental data, ultimately contributing to the design of more damage-tolerant DP steels for automotive applications.

2. Materials and methods

DP 1000 steel, composed of two primary phases, martensite islands dispersed within a ferrite matrix, was selected for investigation. A 1.5 mm thick uncoated steel sheet was selected and procured from Tata Steel (IJmuiden, Netherlands). Table 1 denotes the chemical composition of the material utilised in the study. SEM analysis of the procured material, depicted in Fig. 1, reveals a predominant martensite matrix (dark region-ferrite and bright region-martensite), constituting approximately 51 % of the total volume.

Table 1
Chemical composition of DP1000 steel.

Element	C	Mn	Si	Cr	V	Ni	Nb
Weight %	0.152	1.53	0.474	0.028	0.011	0.033	0.014

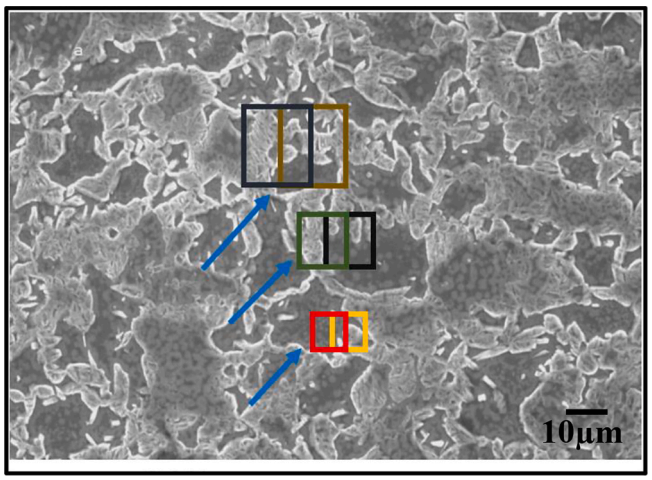

Fig. 1. SEM image of undistorted DP1000 steel with subset size.

2.1. *In situ tensile and bending tests with DIC, and microstructure simulation*

For the in-situ tensile test and bend test experiments, micro specimens were precisely machined according to standard geometry [18,41], as depicted in Fig. 2(a), (b), and (c), respectively. Before loading into the SEM chamber, the specimens underwent a sequential polishing process, starting with abrasive papers of varying grit sizes (P120, P400, P800, and P1200) to eliminate surface scratches, followed by diamond polishing from 6 μm down to 1 μm, to achieve a mirror-like finish essential for high-resolution imaging. To facilitate the visualization of the

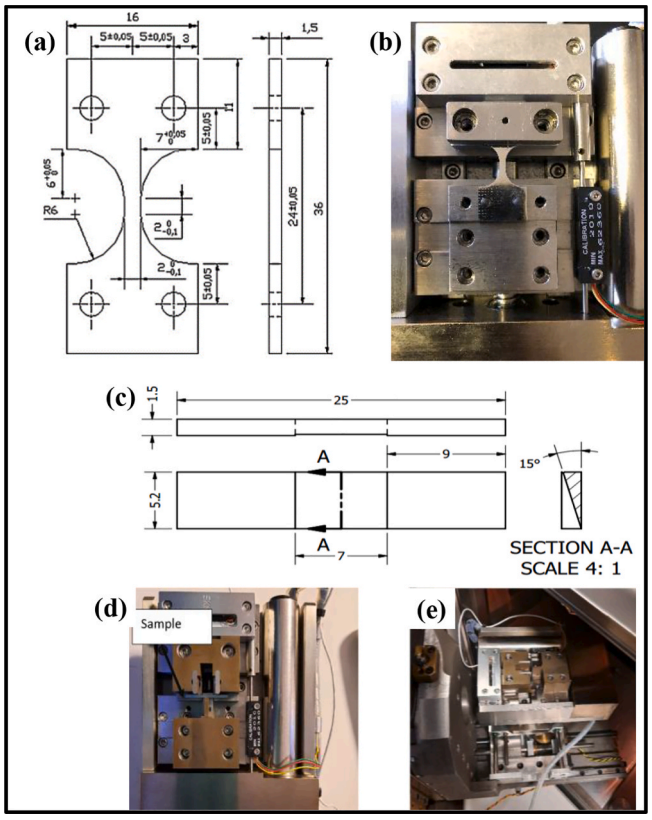

Fig. 2. In-situ mechanical test under SEM (a) Tensile test specimen geometry [11], (b) CamScan SEM image of tensile specimen, (c) Bend test specimen geometry [36], (d) Deben micro bending stage mounted, and (e) CamScan SEM image of bend test specimen.

microstructure during deformation, the specimens were chemically etched using a 2 % Nital solution for 4–12 s. Simultaneously, optical microscopy was employed to verify the microstructure and etching quality, ensuring optimal surface preparation for SEM analysis. The undistorted image was discretized into interrogation windows as illustrated in Fig. 1, with subset sizes ranging from 8 to 32 pixels in LaVision manual [42], extendable up to 512 pixels. These subsets, shaped as spheres, ovals, or squares, may overlap at 0 %, 50 %, or 75 %, influencing displacement calculations. An interrogation window size of 64 × 64 pixels (12.5 × 12.5 μm^2) was selected for this research analysis. A 50 % overlap was applied during the correlation process to improve the resolution of the vector fields, resulting in one deformation vector for every 32 × 32 pixels (6.25 × 6.25 μm^2). Subsequently, true strain values were derived from these vector fields for each interrogation window to generate strain maps based on the reduced passes algorithm [42,43]. A correlation algorithm is then employed to track displacement by identifying unique microstructural features within the interrogation windows.

The prepared tensile test specimens were securely mounted onto a Deben Microtest tensile stage with a 5 kN maximum load capacity for mechanical testing. In total, six fields of view were selected for DIC analysis across different regions of each specimen, covering a combined area of approximately 0.65 mm^2. These areas were chosen to capture statistically representative behaviour across multiple ferrite–martensite configurations and were imaged at 500 magnifications to ensure high spatial resolution for accurate strain mapping. The experiment was conducted under displacement-controlled loading within an SEM chamber under vacuum conditions, maintaining a quasi-static strain rate of 0.1 mm/min. Incremental displacement steps of 0.05 mm were applied, with periodic interruptions to capture high-resolution SEM images, enabling real-time microstructural analysis. Testing continued until fracture, and the acquired images were subsequently processed using DIC strain mapping to quantify localized deformation and strain distribution. Unlike the in-situ SEM tensile experiments, which were conducted in interrupted steps to capture high-resolution images at incremental displacements, the finite element (FE) simulations were performed in a continuous manner. However, to establish a meaningful comparison, the simulation results were sampled at strain values corresponding to the experimental interruption points. This ensured that the stress–strain responses and localized strain fields could be directly compared at equivalent stages of deformation, despite the absence of physical interruptions in the simulation. Accordingly, while the FE model does not replicate experimental pauses, the comparison remains valid as both datasets are aligned at consistent strain levels.

Similarly, the bend test specimens were mounted on the Deben micro-bending stage with a 5 kN maximum load capacity for mechanical testing, as shown in Fig. 2(d). The bending stage was then carefully positioned inside the SEM chamber, as illustrated in Fig. 2(e), under the same conditions as the tensile test. The experiment was conducted to analyze crack propagation within the microstructure using SEM imaging, with deformation and strain distribution further quantified through DIC.

In this study, damage features observed via SEM were classified into two categories: voids and cracks. Voids are defined as small, isolated microcavities typically formed within ferrite regions or along the ferrite–martensite interface before coalescence. Cracks, on the other hand, are sharp, open discontinuities that either initiate independently at phase boundaries or form through the coalescence of multiple voids. This definition was consistently applied during image analysis, DIC correlation, and interpretation of damage progression. Crack propagation, as used in this study, refers to the evolution and extension of both initially nucleated cracks and those formed by coalescing voids under progressive deformation. The observed tensile SEM images were then correlated with finite element (FE) calculations for a comprehensive assessment of deformation and failure mechanisms.

FE simulations were performed in ABAQUS version 2018, the version

available at the University of Sheffield. Although newer versions are available, the fundamental algorithms for reduced-integration elements, hourglass control, and continuum damage modeling employed in this study remain consistent. Verification and validation procedures, including mesh convergence studies, calibration of phase-specific material properties, and comparison with experimental DIC and load–displacement data, were conducted to ensure accuracy, robustness, and reproducibility of the simulations.

Fig. 3 illustrates the workflow for generating stress maps from the obtained microstructure using MATLAB and Abaqus software [27,44,45]. The process begins by dividing the SEM microstructure images into subset windows using MATLAB code, as shown in Fig. 1, and converting them into black-and-white images using the Chalon window technique [46]. The code partitions the image into smaller segments and transforms each segment into a square unit consisting of four nodes. For the FE simulation, a linear quadrilateral element (CPS4R) with a two-dimensional (2D) meshing approach was employed. The elastic modulus values for ferrite and martensite were set at 198 GPa and 182 GPa, respectively, with a Poisson's ratio of 0.3 for both phases [47–50]. Boundary conditions were derived from DIC results, and a MATLAB script was used to define the stress domains, which were subsequently imported into Abaqus for simulation.

The DIC analysis provided displacement values in the X and Y directions, along with corresponding coordinates, for the entire image. However, since the region of interest was the SEM image, the MATLAB code extracted only the displacement data corresponding to this specific area. These extracted displacements were then assigned as boundary conditions for the analyzed region. In Abaqus, stresses are computed at integration points within each element and subsequently extrapolated to the nodes for visualization and averaging. In this study, the nodal stress values refer to these extrapolated results rather than stresses directly computed at the nodes. The finite element model incorporates a greater number of elements than the available subsets of DIC results. This implies that multiple nodes within the FE model correspond to the interval between two DIC data points. There are seven nodes situated between consecutive DIC data points, as depicted in Fig. 4. The MATLAB script also allowed specification of the model nodes where the DIC displacement results were to be applied.

Two sets of microstructural simulations were performed based on the boundary condition application method. In the first set, all nodes in the model were assigned X and Y displacements, resulting in a fully constrained simulation intended to closely replicate the actual deformation of the analyzed region. This approach assumes a perfectly cohesive interface between ferrite and martensite. In the second set, boundary conditions were applied only to the edges of the simulated microstructure, with displacement values along these edges extracted and interpolated from the DIC data. The remaining nodes were left free to deform according to their respective phase properties. The average stress for the analyzed microstructure was then calculated using Eq. (1).

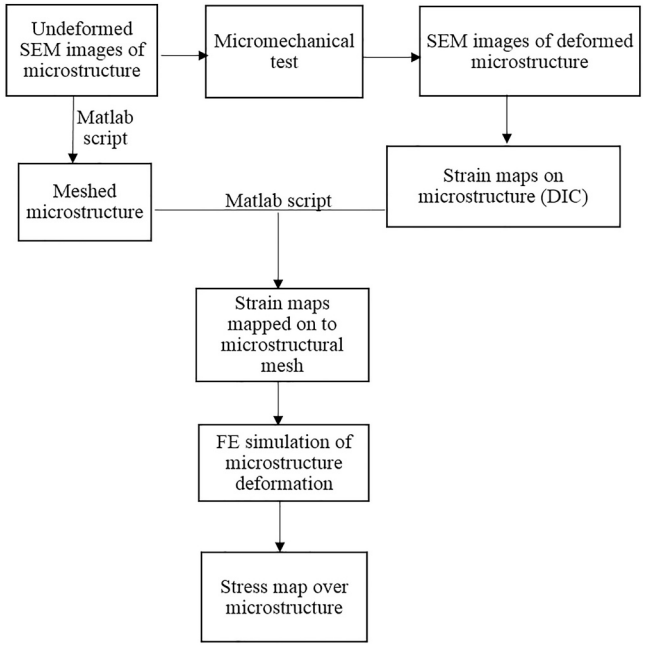

Fig. 3. FE simulation methodology flowchart.

$$\overline{\sigma} = \frac{1}{V}\int_V \sigma \, dV \tag{1}$$

where $\overline{\sigma}$ is the stress average, V is the total area of the microstructure model, and σ is the stress computed at every node after extrapolation from the integration point. Subsequently the microstructure was modeled on the sample surface, where the out-of-plane stress is negligible, the simulation was performed under a two-dimensional plane stress condition with a unit thickness [51–53]. The volume integration in the original formulation is therefore appropriately converted to an area integration, consistent with the 2D analysis. The Maximum principal stress was averaged over all elements in the mesh using equation (1). The resulting stress distributions were then analyzed to correlate with damage initiation and propagation mechanisms in DP 1000 steel, providing insights into its mechanical behavior under loading conditions.

2.2. Continuum damage modeling of DP1000

To understand plastic work hardening and improve void growth prediction, GTN-based damage modelling was calibrated via FE simulations and validated against the in-situ SEM tensile test geometry [28,31,35,36]. In this research, the continuum damage modelling (GTN model) involves modelling the deformation of a macroscopic specimen until the point of fracture is reached. The GTN model is simulated using Abaqus software based on Eq. (2) [54–57]. The yield of ductile fracture can be expressed as follows:

$$\Phi = \frac{\sigma_{eq}^2}{\sigma_y^2} + 2fq_1 f^* \cosh\left(\frac{q_2}{2}\frac{\sigma_{kk}}{\sigma_y}\right) - 1 - q_3 f^{*2} = 0 \tag{2}$$

where q_1, q_2 and q_3 are the damage parameters, in most materials, the constant q_1 ranges from 1.0 to 1.5, and q_2 equals 1.0 [29,30,33,56–58]. σ_{kk} is the stress-tensor trace, σ_y is the yield strength, and σ_{eq} is the von Mises equivalent stress (see Eqs. (3)–(6)) [54,55]. In this formulation, the von Mises equivalent stress (σ_{eq}) which is integrated over the domain to obtain a representative measure of the average stress state. The use of von Mises stress is justified as it provides a scalar quantity that characterizes yielding in ductile metals and allows meaningful comparison between experimental and numerical results.

$$\sigma_{kk} = \sigma_1 + \sigma_2 + \sigma_3 \tag{3}$$

$$\sigma_{eq} = \sqrt{\frac{1}{2}\left[(\sigma_1 - \sigma_2)^2 + (\sigma_2 - \sigma_3)^2 + (\sigma_3 - \sigma_1)^2\right]} \tag{4}$$

$$f = 1 - r \tag{5}$$

$$r = \frac{V_m}{V_t} \tag{6}$$

Where f is the current void volume fraction, f^* effective void volume fraction, V_m is the matrix volume and V_t is the total volume of the material. The failure model must effectively define the material behaviour up to the point of fracture. In the case of f = 1, the material is made up of voids only, and rupture will occur. For f = 0, the material is completely dense, and Eq. (7) of the yield can be redrafted as:

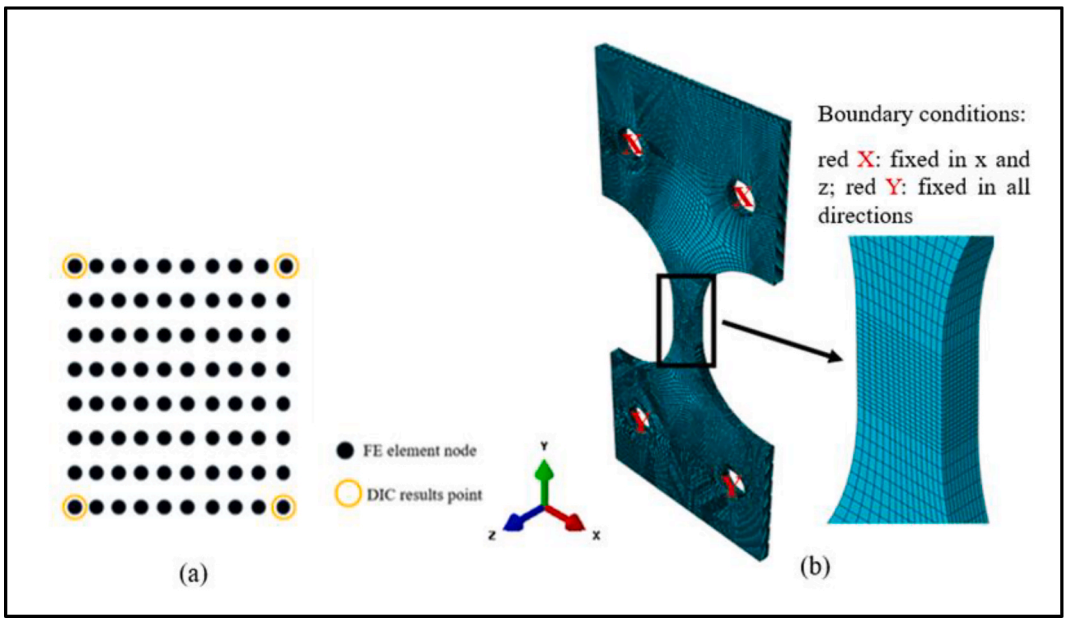

Fig. 4. (a) Demonstrates the node numbers in the microstructure model located between the DIC points. (b) Finite element model of the SEM tensile sample geometry.

$$\Phi = (\frac{\sigma_{eq}}{\sigma_y})^2 - 1 = 0 \tag{7}$$

which shows that the undamaged material is a von Mises material. Needleman and Tvergaard [57] studied void coalescence and introduced the multiplicative fraction δ, which predicts the acceleration rate of the void growth through the effective porosity. The effective porosity f^* can be defined as follows:

$$f^* = \begin{cases} f, f < f_c \\ f_c + \delta(f - f_c), otherwise \end{cases} \tag{8}$$

where f_c is the critical porosity at which the void begins to coalesce; f_c and δ can be identified through experimentation [57]. A simple phenomenological foundation can be presented for void nucleation in strain-controlled nucleation, and can be expressed as Eq. (9).

$$\dot{f_n} = A_n \dot{p} \tag{9}$$

where A_n is the strain-controlled nucleation and depends on the parameter p, which denotes the plastic strain as in Eq. (10).

$$A_n = \frac{f_n}{s_n\sqrt{2\pi}} exp\left(-\frac{1}{2}\left(\frac{p-\varepsilon_n}{s_n}\right)^2\right) \tag{10}$$

This relationship illustrates certain parameters. f_n denotes the inclusion volume fraction of void which can be nucleated; ε_n denotes the strain where 50 % of the particles are broken; s_n denotes the standard deviation of the nucleation strain. Validation is performed by comparing the model prediction against the load–displacement curve in the tensile test carried out in the SEM. The true stress–strain curve for DP1000 was obtained experimentally from tensile testing. It was introduced into the Abaqus software to simulate the tensile deformation of SEM specimens. Plastic deformation and damage were simulated using the Gurson damage model, and the linear C3D8R element type was implemented for the meshing as shown in Fig. 4 (b).

For the situ tensile test modelling, the boundary conditions were such that the two bottom holes of the sample as shown in Fig. 2(a) and. Fig. 4 (b) were fixed in all directions except for the rotation around the Z axis (because it is an out-of-plane axis), which was designed to stimulate boundary conditions in the application of a real test through an experiment, whereas the two top holes were fixed in the horizontal and out-of-plane directions (X and Z axes). Afterwards, a linear speed (0.001 mm/s) was utilised in the Y direction to recreate the conditions in the actual experiment. As the speed was low, the model could be run in a quasi-static state. The model was discretised using linear 3D C3D8R solid elements. Since reduced integration elements were employed, Abaqus' enhanced hourglass control was utilized to prevent non-physical zero-energy deformation modes, ensuring numerical stability while accurately capturing local stress and strain fields. Mesh refinement was applied in critical regions expected to experience high-stress gradients, such as around the holes and near the gauge section, to accurately capture local stress concentrations. Coarser elements were used in less critical regions to reduce computational cost. A mesh convergence study was performed to confirm that the simulation results, including local stress and strain distributions, were independent of element size. Critical regions with high stress gradients, such as around holes and the gauge section, were refined to accurately capture stress concentrations, while coarser elements were maintained in regions of lower gradients to optimize computational cost. The mesh convergence study was performed to confirm that the simulation results, including local stress and strain distributions, were independent of element size. Critical regions with high stress gradients, such as around holes and the gauge section, were refined to accurately capture stress concentrations, while coarser elements were maintained in regions of lower gradients to optimize computational cost. The mesh convergence studies were performed to ensure that the results were independent of element size. The finite element model was validated by comparing global load–displacement responses, local strain distributions from DIC, and observed fracture locations. The close agreement between experimental and numerical results confirms the reliability and physical accuracy of the simulations.

Fig. 4 illustrates the overall mesh, and the refined regions have been included to provide a clear visual representation of the meshing strategy. Therefore, to model the material behaviour of the softening part, the static analysis was also used in Abaqus/CAE. The parameters of the Gurson model, q_1 and q_2 , were recommended by [56] to obtain the best match for the experimental load–displacement curves of the typical materials. The void nucleation parameters f_n, ε_n and s_n were selected according to the Abaqus manual for typical materials [44].

3. Results

3.1. In-situ tensile behaviour and microstructural evolution in Dual-Phase steel

In-situ SEM images were captured during the tensile test by interrupting the extension every 0.05 mm to understand the damage phenomenon of DP steel, including local deformations, damage initiation, and propagation to the point of specimen fracture, as represented in Fig. 5.

(i) Localized Plastic Deformation

Fig. 5 (A) and (B) show micrographs capturing the early stages of plastic deformation in the material, with an applied strain of 0.11 Ɛ and 0.18 Ɛ, respectively. At this stage, localized deformation is evident, particularly within large ferrite grains (Fig. 5 (B)), which contrasts with smaller ferrite regions trapped between islands of martensite. Notably, the ferrite phase begins to deform before any cracks appear in the martensite. The localized plastic deformation is initially concentrated in the ferrite and martensite phases. As strain progresses, Fig. 5 (C) and (D) illustrate how this localization leads to the development of damage, with the strain reaching approximately 0.35 Ɛ at the point of failure. The enlarged regions in these figures highlight the proliferation of plastic deformation within both the ferrite and martensite phases, with the most intense deformation occurring in the larger ferrite regions (marked by ovals in Fig. 5 (A-D)). This intense localized deformation eventually causes the separation of martensite islands, particularly visible in the rectangular and oval regions of Fig. 5. (C) and (D). The SEM analysis of the microstructure reveals void nucleation in DP1000 steel, primarily occurring in the ferrite phase near the ferrite-martensite interface following significant plastic deformation. As deformation continues, damage propagation leads to cracking in the martensite phase. Fig. 5 (C') highlights instances of void development near martensite islands as strain increases. Void initiation is visible in Fig. 5 (C') at a strain of 0.3 Ɛ, with damage spreading into the adjacent ferrite phase, where the now-separated martensite island is located. The following sections provide a detailed explanation of these deformation and damage mechanisms.

(ii) Inspection of martensite cracks and ferrite voids.

According to Rashid [59] and Tasan et al. [60], damage in the martensite phase is typically induced by high stress, while damage in the ferrite phase is primarily driven by high strain. The current analysis reveals martensite cracking occurring at different stages across the microstructure. Fig. 6 provides stress–strain data, showing an interruption every 0.05 mm of extension to track microstructural deformation and martensite cracking until failure.

The observed damage mechanisms include:

- Martensite cracking (Crack 1): Martensite deformed until cracks formed, with a global strain of 0.0486 Ɛ and stress of 1020.5 MPa just before crack initiation, as shown in Fig. 6 (a).
- Ferrite deformation near martensite cracking (Cracks 2 and 3): Ferrite deformed near the martensite crack at a strain of 0.11 Ɛ and stress of 1050.8 MPa before UTS, leading to crack 3 after the UTS at a strain of 0.13 Ɛ and stress of 1053 MPa (see Fig. 6 (b) and (c) respectively).
- Void formation in ferrite: Large deformation in the ferrite phase near the ferrite-martensite interface led to void nucleation (Crack 4), with stress at 892 MPa and strain at 0.3 Ɛ (see Fig. 6 (d)).

These mechanisms demonstrate that martensite cracking can occur at low strain levels (mechanism 1) but typically follows significant strain localization at or near the interface (mechanism 2). Mechanism 3, involving martensite cracking after large strain in ferrite, was rarely observed. Cracks formed between strain values of 0.05 Ɛ and 0.3 Ɛ, with failure occurring at a strain of 0.35 Ɛ. Notably, voids in the ferrite phase, which are rarely reported in tensile testing, were observed in this study. These voids formed under high global strain rates, eventually propagating to cause martensite cracking. The first void, initiated at a global strain of 0.26 Ɛ, was surrounded by martensite, while a second void grew with limited propagation before final fracture.

(iii) DIC Analysis: Strain Distribution

Continuous DIC analysis was employed to track deformation and damage evolution within the microstructure. Fig. 7 shows the strain distribution (Exx – Lagrangian strain, along the tensile axis) superimposed on the deformed SEM micrographs. Early plasticity was

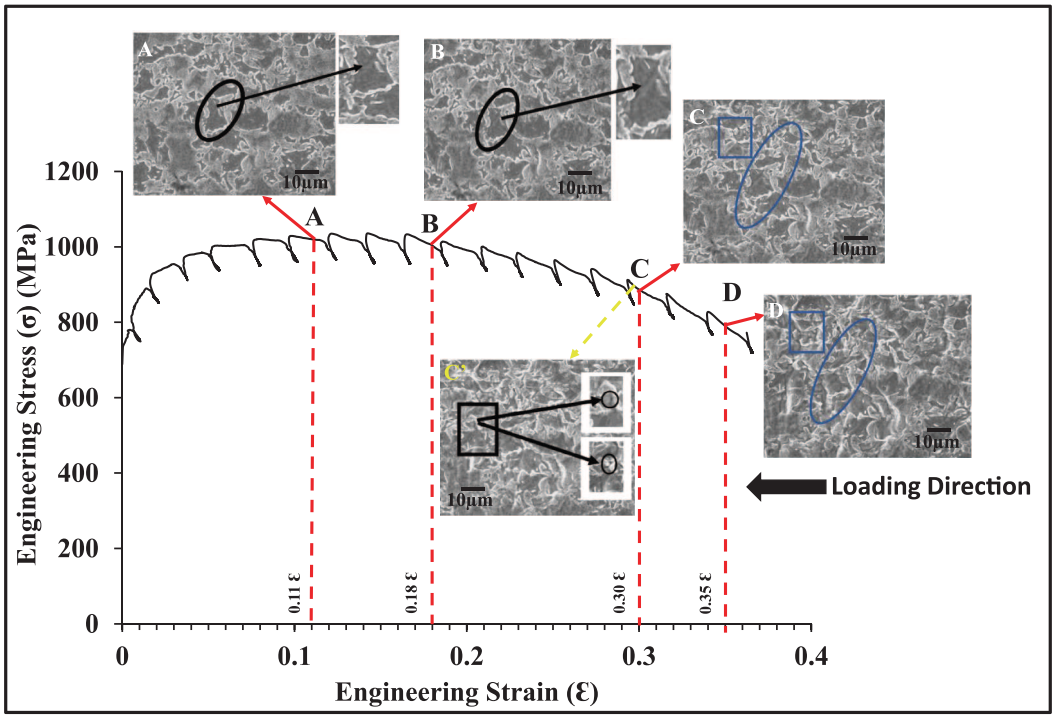

Fig. 5. In-situ tensile test and microstructure analysis under SEM.

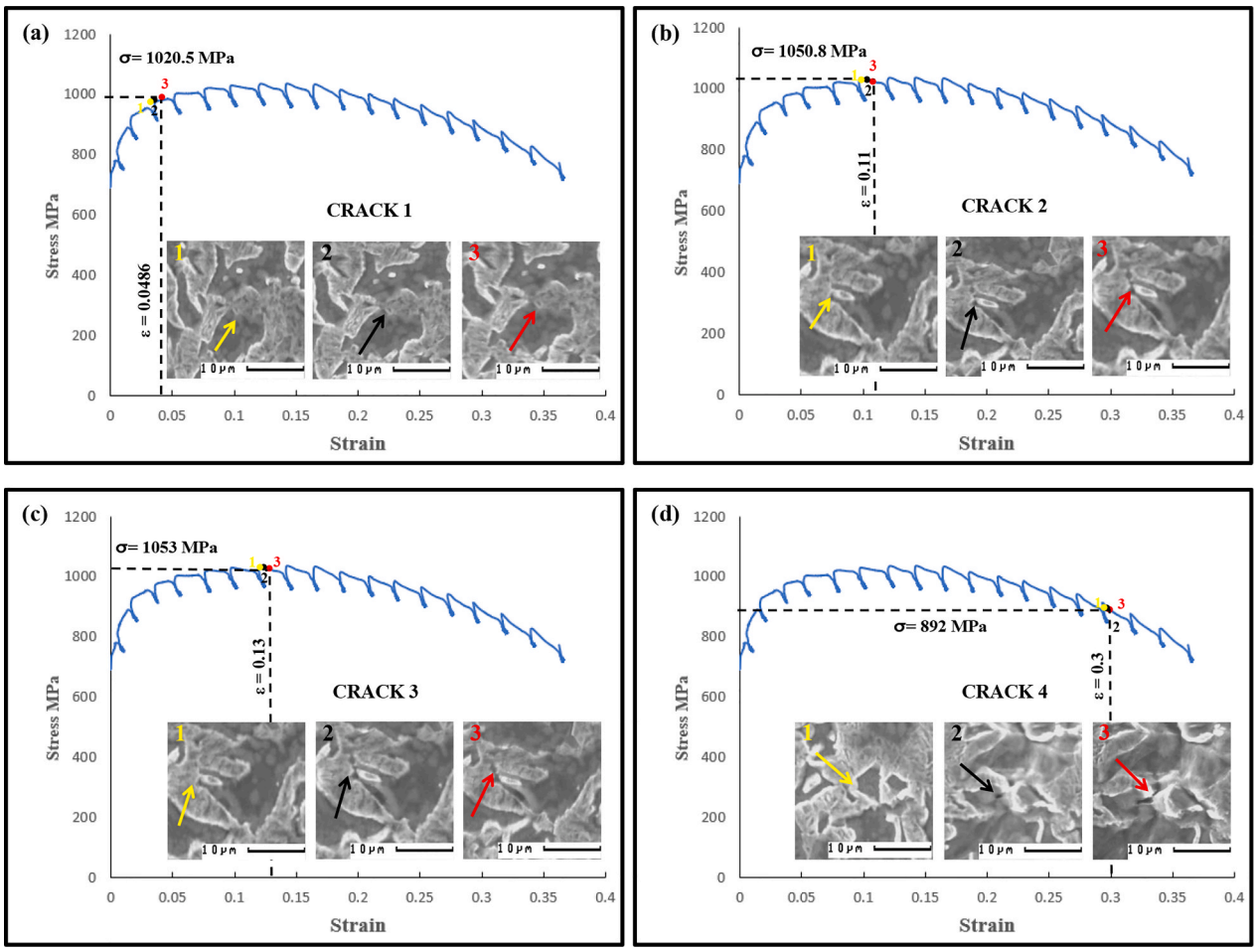

Fig. 6. Martensite cracks and void formation mechanism at different strain (a) 0.0486 Ɛ, (b) 0.11 Ɛ, (c) 0.13 Ɛ, (d) 0.3 Ɛ.

detected in the ferrite phase at a global strain of 0.01, forming localised deformation bands (Fig. 7 (A) and (B)). Peak local strain values of ~ 0.018 were initially observed in ferrite, while martensite remained mostly undeformed, except where adjacent to localised highly strained ferrite regions, as shown in Fig. 7 (O).

At UTS (1053 MPa, global strain 0.13 Ɛ), Fig. 7(A') reveals intense strain localisation in ferrite-dominated areas (areas 1 and 3), with maximum strains up to 0.3 Ɛ. Strain maps at higher strains (0.18 Ɛ and 0.33 Ɛ global strain, Fig. 7 (B) and (C)) show the intensification of deformation bands, with ferrite reaching localised strains of 0.55 Ɛ and up to 2.5 Ɛ before final fracture. Martensite generally exhibited lower strain (~ 0.1), reflecting significant strain heterogeneity between and within phases. Notably, deformation bands initiated in ferrite propagated across martensite, often serving as precursors to crack formation. The strain frequency distribution at UTS was obtained from combined DIC mapping and FE simulations using MATLAB and Abaqus (Fig. 8(a) and 8(b)). These results show that ferrite and martensite exhibit similar average strains (0.11 and 0.10, respectively) and comparable heterogeneity. However, localized strain analysis (Fig. 8(c)) reveals that ferrite consistently accommodates slightly higher local strains, especially near ferrite–martensite interfaces, where geometric and mechanical incompatibilities induce stress concentrations that promote void nucleation and early-stage damage.

This localized strain accumulation in ferrite, particularly after UTS, indicates that ferrite deformation dominates microstructural damage initiation, even when average strains appear similar across phases. These observations demonstrate that average strain alone can underestimate the role of microstructural heterogeneities and emphasize the need for spatially resolved strain analysis to accurately capture damage mechanisms. The results provide an automatous link between microscale strain localization and macroscopic fracture, highlighting the critical role of ferrite–martensite interactions in the overall failure process of dual-phase steel.

(iv) DIC Analysis: Martensite Microcracking and Ferrite Void Nucleation

Fig. 9 presents strain maps immediately before martensite fracture. The first crack nucleated at a local strain of 0.088, close to the region of highest strain. Most martensite cracks, such as crack 4, originated adjacent to high-strain ferrite zones near the ferrite–martensite interface, with local strains ranging from 0.33 to 1.48. It is important to note that the maxima represent localized peaks in strain distribution rather than the exact locations where cracks initiate. For instance, cracks 2 and 4 were observed to initiate at intermediate strain values (0.15–0.2), which are lower than the absolute maxima indicated in the red regions of the DIC strain maps on the SEM microstructure images. This distinction emphasize that fracture initiation is influenced not only by peak strain but also by local microstructural features, strain gradients, and phase interactions, particularly near ferrite–martensite interfaces, where mechanical incompatibilities promote void nucleation and early-stage damage.

Despite increasing global strain, the majority of martensite fractures initiated when local strains reached 0.15– 0.33. Ferrite void formation was also strain-mapped, consistently nucleating at localised strain values of ~ 1.04, adjacent to martensite regions. Strain fields (Fig. 7) showed that deformation bands, once formed, remained stationary. Eight out of twelve martensite cracks initiated at these persistent high-strain sites, highlighting the critical role of ferrite strain localisation in martensite fracture. Fig. 10 (a) shows a clear trend of increasing local

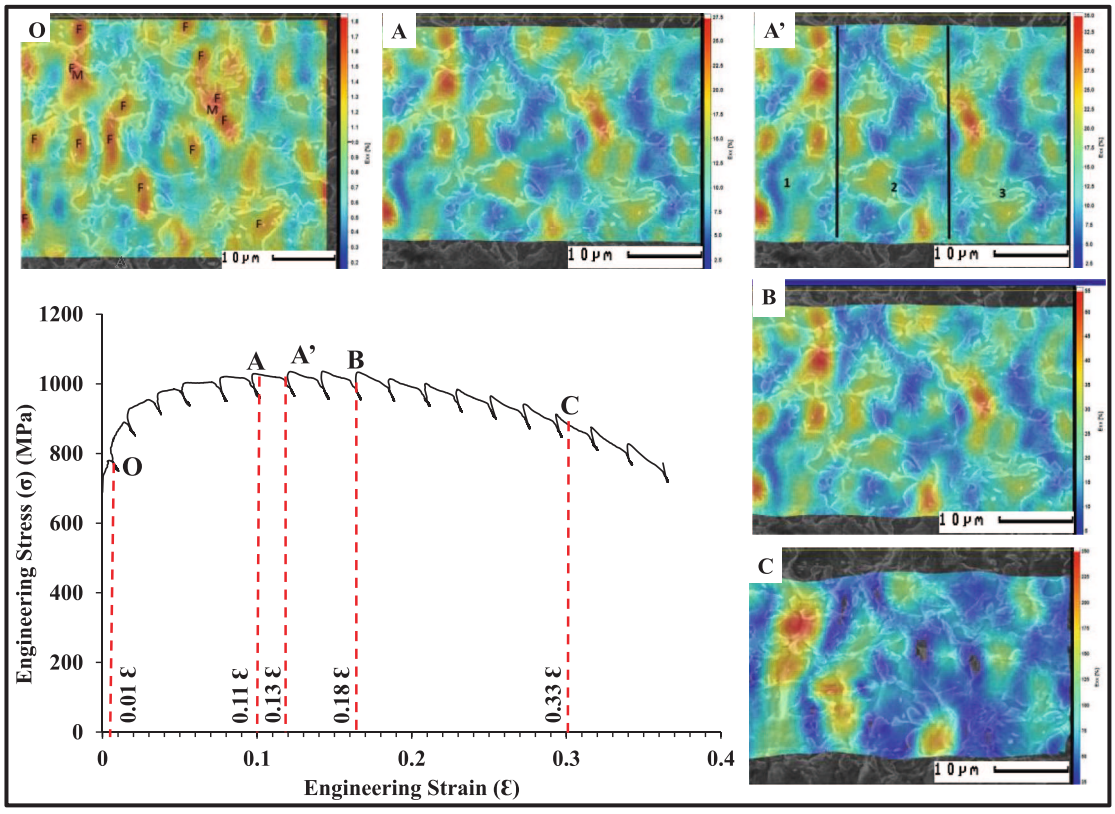

Fig. 7. In-situ Tensile Test DIC analysis at different strain values: (O) Origin of plastic deformation in ferrite region at 0.01 Ɛ, (A) 0.11 Ɛ, (A') 0.13 Ɛ, (B) 0.18 Ɛ, and (C) 0.33 Ɛ just before failure.

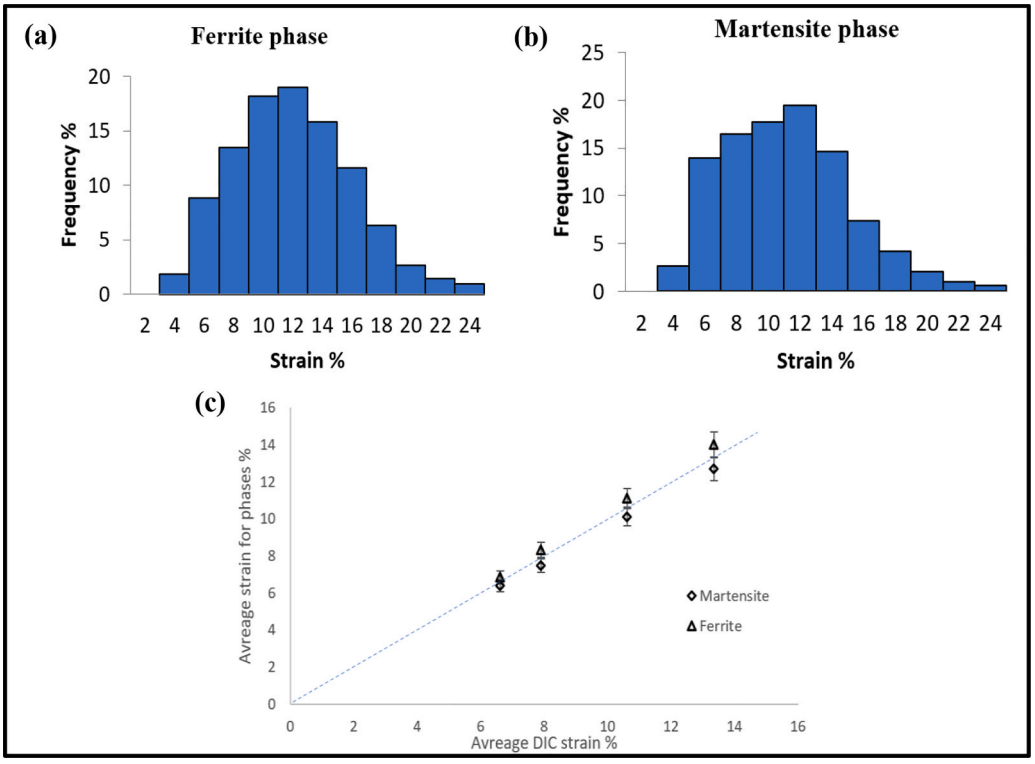

Fig. 8. Strain values histogram (a) Ferrite phase, (b) Martensite phase, and (c) Evolution of strain partitioning between ferrite and martensite.

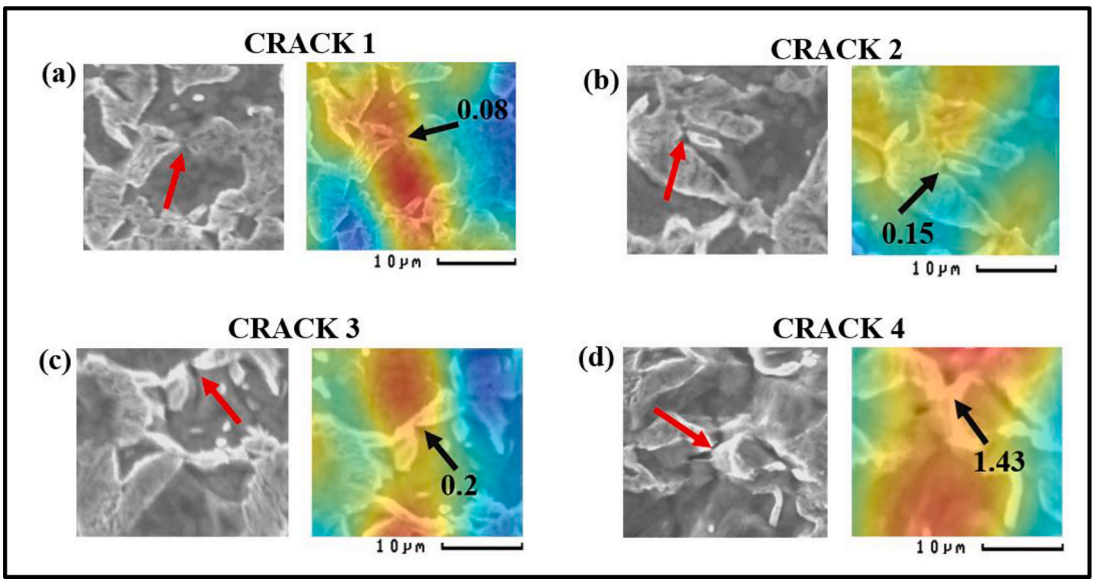

Fig. 9. Strain distributions to the onset of the martensite cracking (a) Crack 1, (b) Crack 2, (c) Crack 3, and (d) Crack 4 mechanism.

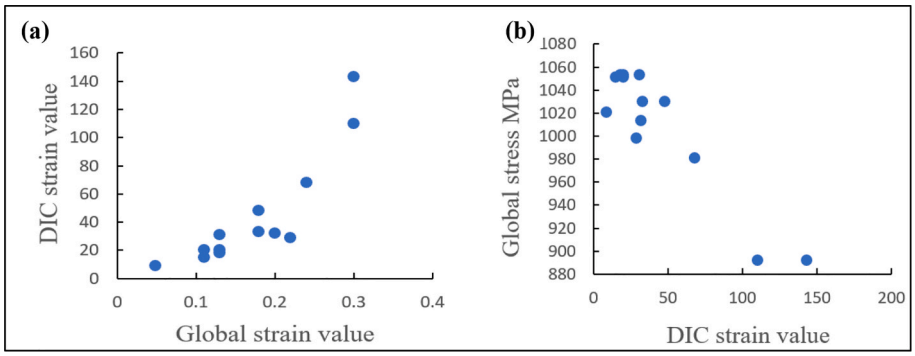

Fig. 10. (a) Global strain value vs local DIC strain values, and (b) Global stress value (MPa) vs the local DIC strain value.

strain correlating with global strain at martensite fracture initiation, primarily around the UTS. Similarly, Fig. 10 (b) links global stress levels with local strain values at cracking sites, confirming that martensite failure is predominantly strain-driven and occurs near peak global stress. Fig. 10(b) reveals that most data points cluster at high global stress levels (~1000–1060 MPa) with relatively low strain (~0–50), while a smaller subset exhibits markedly higher strain (100–150) at lower stress (~880–900 MPa). This distribution emphasizes the critical role of strain localization and microstructural heterogeneities in governing martensite cracking and indicates that, in the present study, martensite fracture is largely strain-driven.

This strain-driven mechanism contrasts with earlier works that identified high local stress concentrations as the primary trigger for martensite cracking in dual-phase steels [1,6]. It underscores the importance of local strain accumulation and heterogeneous plastic deformation within martensite, as also highlighted in microscopic DIC and EBSD-based strain mapping studies [11,18]. Such insights have significant implications for constitutive modeling: rather than relying solely on global stress thresholds or stress triaxiality, predictive models may need to explicitly incorporate strain localization and microstructural constraints [8,38,39]. The divergence from stress-driven fracture reported in prior studies may arise from variations in ferrite–martensite morphology, phase connectivity, and volume fraction [61], as well as experimental factors such as strain rate sensitivity [13,16], loading mode, and testing temperature [2,5]. Situating these findings within the broader literature highlights that both stress- and strain-driven mechanisms can operate depending on microstructural and testing conditions, and the present results extend this understanding by demonstrating a scenario in which strain accumulation dominates martensite failure.

(v) FE Simulation Analysis.

The deformation and damage mechanisms in DP1000 during in-situ SEM tensile testing were further analysed using modelling analysis. FE simulations, performed in Abaqus, provided stress distribution data across the ferrite–martensite microstructure that could not be directly measured experimentally. Microstructure-based modelling focused on crack initiation in martensite and void nucleation in ferrite.

The accuracy of the simulations depends on the mesh size and corresponds to the subset (square) size used to discretize the SEM images. It was therefore vital to study how the subset size affected the resolution of the geometry phases, as simulated in the finite element model, in particular, how this would affect the microstructure simulation results. A fine mesh size would provide microstructure simulation results that would match the experimental results best. However, when the element size was small, the FE microstructure shape deformation was indeed very close to that included in the experimental results.

Fig. 11 represents how changing the subset size, discretising the SEM image, affected the resolution of the image itself, and Fig. 12 details the effect on the resolution of the phase geometry, as simulated in the finite element model. A mesh size corresponding to 1 pixel in the image was selected for this study.

A mesh convergence analysis was further conducted on the

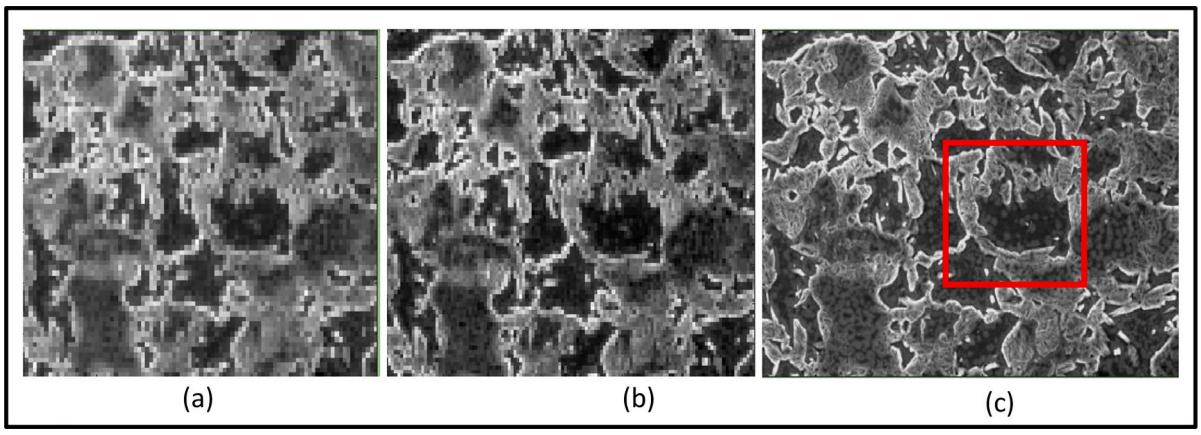

Fig. 11. Effect of the subset size on the image resolution: (a) 8 x 8 pixels, (b) 5 x 5 pixels, and (c) 1 square pixel.

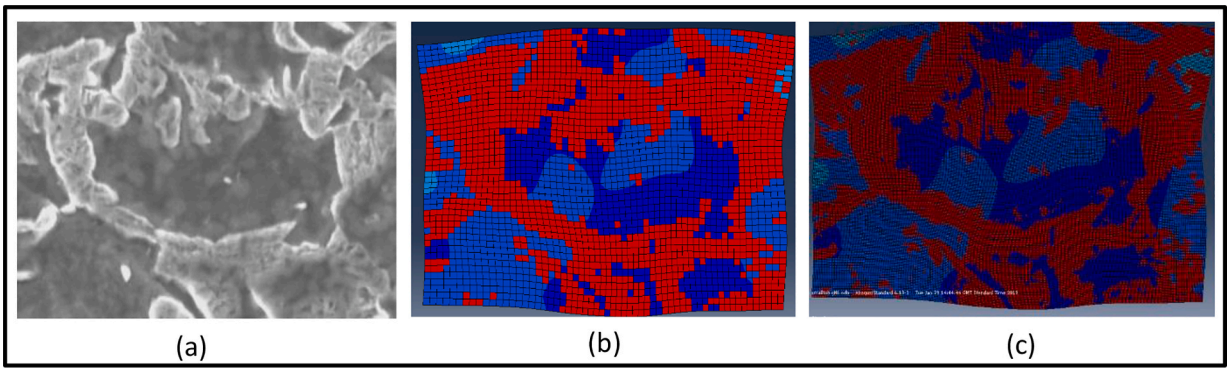

Fig. 12. (a) Area of the microstructure highlighted by the red rectangle in Fig. 11 (c), (b) Mesh corresponding to a 5 x 5 pixels subset size, and (c) 1 pixel subset size. (For interpretation of the references to colour in this figure legend, the reader is referred to the web version of this article.)

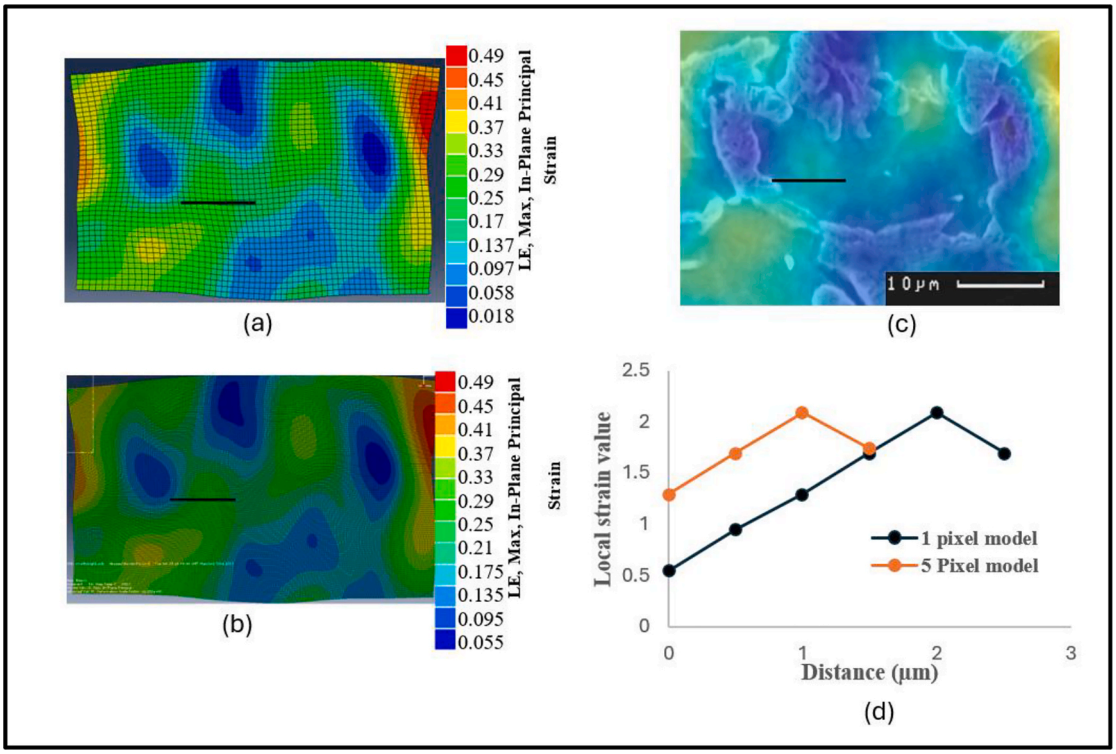

Fig. 13. (a) Five-pixel model showing the maximum principal local strain distribution, (b) One-pixel element size showing the maximum principal strain distribution, (c) SEM image with a black line indicating the location where the strain distribution was measured, (d) Plot of the maximum strain along the black line.

microstructure models, with boundary conditions applied at the edges, to compare their mechanical response with experimental results. Local strain was evaluated along a measurement line drawn from martensite toward ferrite (Fig. 13). It was found that an element size corresponding to one pixel provided higher resolution and a smoother strain distribution than five pixels, indicating that the results were sufficiently mesh-independent. These observations are consistent with prior work showing that martensite size and morphology strongly influence strain distribution and micro-damage evolution in DP steels, particularly when comparing segregation-neutralised and banded grades [62]. Additionally, hourglass control was implemented in Abaqus to prevent zero-energy modes in the reduced integration elements (CPS4R), ensuring stable and physically meaningful deformation results. V&V efforts were also carried out using the FE simulations were systematically checked for mesh dependency, element size effects, and convergence of stress/strain distributions. Comparison of numerical results with experimental flow curves and DIC strain maps confirmed the accuracy of the model and its predictive capability for local stress, strain, and damage evolution.

The flow curves for the martensite and ferrite phases had to be adjusted to correspond to the literature, to minimise the error between the simulation and experimental results [27]. Microstructure simulation was undertaken to calibrate the phase properties for this work. The Poisson ratio for both phases was 0.3, and the moduli for elasticity were 182 GPa for the martensite and 198 GPa for the ferrite. The SEM image shown in Fig. 1 was used for the purposes of the simulation. Global strain values of 0.017, 0.032, and 0.048 were utilised because no damage was observed at the level of applied strain located before the UTS.

The flow curves for the martensite and ferrite were adjusted by minimising the difference between the computed (see equation (1) for the computation of the average stress) and measured flow stress values [27]. Fig. 14 details the curves adjusted for the ferrite and martensite phases that resulted from this calibration procedure, and Table 2 reports the error values between numerical and experimental flow stress values. The minimum error was found to be 1.08 %.

It is important to note that, although the in-situ SEM tests included multiple interruptions during loading to capture microstructural evolution, the finite element (FE) simulations were conducted continuously without explicit pauses. To reconcile this difference, the FE results were extracted at strain levels corresponding to the experimental interruption points, providing a consistent framework for meaningful comparison between experimental and numerical observations. The results in Table 2 reveal that there is an acceptable error between the true experimental stress and the average stress from the simulation. The adjusted flow curves were therefore used in subsequent simulations to analyse stress distributions at the onset of damage to the microstructure. The next step concerning the microstructure simulations was to check that the displacement vectors measured through DIC were correctly

Table 2
Percentage error between the experimental true stress and averaged simulation stress for applied displacements selected before the appearance of the first crack.

Applied strain	0.017	0.032	0.048
SEM true stress (MPa)	1110	1138	1170
Average simulation stress (MPa)	1098	1107	1133
Error %	1.08	2.7	3.16

transferred as boundary conditions for the finite element simulations describing the deformation of the microstructure aimed at analysing the onset of damage nucleation. Strain distributions were measured by DIC and predicted with the finite element model and then compared. Fig. 15 shows this comparison, and Table 3 shows the error between the experimental DIC strain and the simulated strain values for particular locations on the maps. The level of error associated with the maximum strain value was 3.1 %, which is considered acceptable.

After verification of the strain results, FE simulations were conducted to assess the stress distributions in the martensite and ferrite phases of DP1000. These simulations aimed to analyse the local stress resulting in damage to the microstructure.

The image selected for this study was captured prior to the appearance of the first, second, and third cracks in the martensite. This made it possible to analyse the local stress values before the onset of the martensite cracking phase. The microstructure analysis corresponded to a global strain value of 0.048. The analyses then continued for a small area, including about six cracks within the martensite region. SEM observations identified a small area where six martensite cracks developed during deformation (Fig. 16 (a)). Experimental DIC results showed that cracking often correlated with high local strain regions in ferrite. Fig. 16 (a) presents the experimental strain map at a global strain of 0.11, with black lines marking martensite cracking sites, while Fig. 16 (b) shows the simulated maximum principal stress distribution, with high-stress areas highlighted.

Cracks typically initiated in martensite regions experiencing maximum principal stresses up to 1783 MPa, though not all high-stress regions resulted in cracking. Stress distributions were also analysed for ferrite void nucleation. Experimentally, voids initiated at global strains of 0.26–0.3, corresponding to local strains of 0.75–1.41 as tabulated in Table 4. Fig. 16 (c) shows an example of a ferrite void and its associated stress field before void nucleation. Voids consistently formed in regions of elevated stress, with maximum principal stresses ranging between 915–990 MPa (refer to Table 4).

(vi) GTN modelling and stress–strain Analysis.

FE modelling was presented to study the deformation and damage behaviour of dual-phase steel. The damage modelling was conducted using the GTN model, with the model parameters calibrated using FE simulation. Furthermore, validate the model against the in-situ tensile specimen geometry for the test conducted in SEM. The predictability

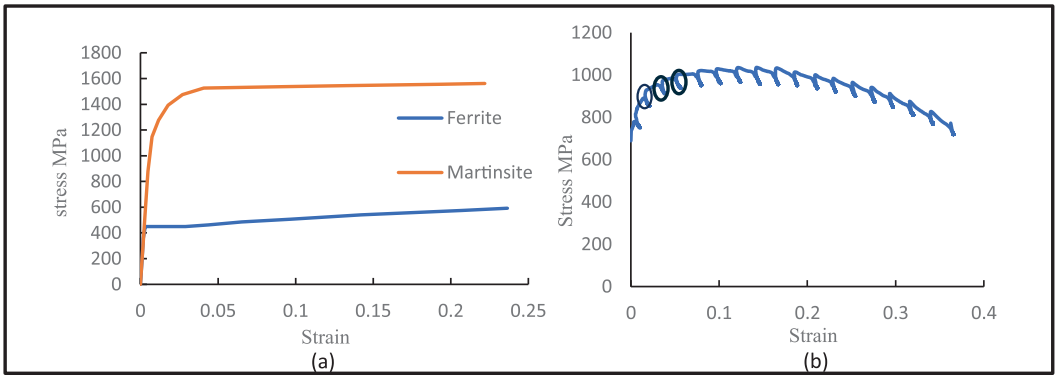

Fig. 14. (a) Adjusted stress–strain curves for both phases from finite simulations of the microstructure, (b) Applied strain values selected for calculated errors reported in Table 2.

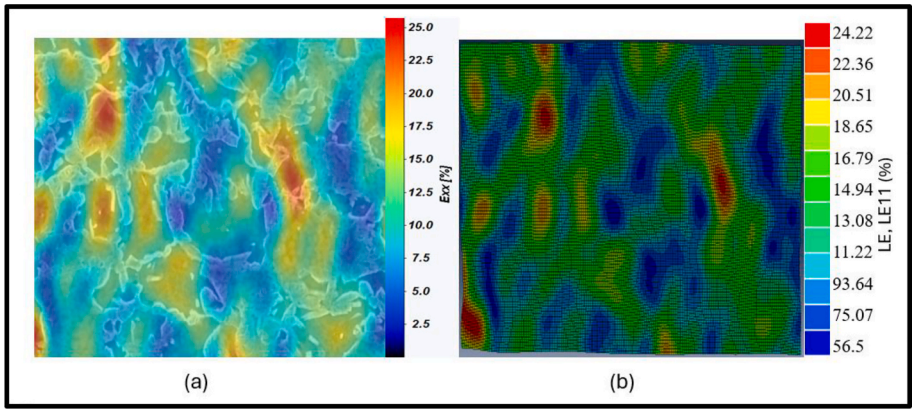

Fig. 15. Strain distributions for (a) Experimental, and (b) Modelling results.

Table 3
Error between experimental and simulation strain values.

Experimental strain (DIC)	25	22.5	20	17.5	15	12.5
Simulation strain	24.22	21.74	19.2	16.79	14.31	11.84
Error (%)	3.11	3.35	3.65	4.04	4.55	5.27

capacity of the Gurson model with q parameters calibrated with the SEM tensile geometry was then tested for validation purposes against the load displacement curve recorded during the in-situ tensile test inside the SEM. The standard deviation and volume fraction for the FE GTN simulations are $S_n = 0.06$ and $f_n = 0.05$. The mean value in the continuum GTN model is $\varepsilon_n = 0.3$,. Close agreement is observed here, thereby validating the previously identified parameters as represented in Table 5. Furthermore, Fig. 17 shows that an even closer match can be achieved when adjusting the value of the mean and volume fraction parameters while keeping the q parameter values constant (q1 = 1.6, q2 = 1.1, and q3 = 2.56).

The comparison in Table 5 indicates that the q_1 and q_2 parameters obtained from the SEM-based calibration are slightly higher than those from the general GTN model, suggesting a marginally greater influence of stress triaxiality in the SEM-tested geometry. Similarly, the higher f_n and S_n values for the SEM calibration reflect a broader distribution and higher initial volume fraction of void nucleation sites, which can be attributed to the localized stress and strain fields captured during in-situ testing. In contrast, the identical ε_n value in both cases implies that the average strain for void nucleation remains consistent, regardless of the

Table 4
Ferrite void initiation.

Void number	**Global strain value**	**Local strain value**	**Local stress value (MPa)**
1	0.26	104 %	921
2	0.26	104 %	923
3	0.3	141 %	990

Table 5
Comparison of GTN and SEM parameters.

Parameters	q_1	q_2	f_n	ε_n	s_n
GTN	1.5	1	0.04	0.3	0.05
SEM	1.6	1.1	0.06	0.3	0.06

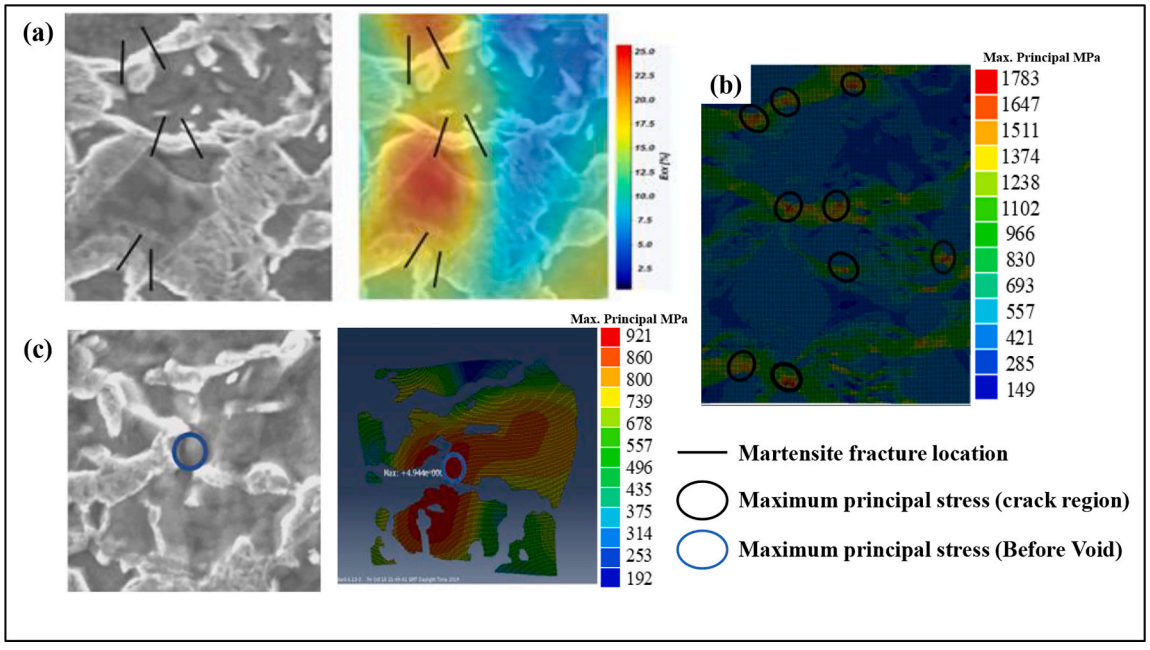

Fig. 16. FE simulation (a) Martensite crack strain values, (b) Maximum principal stress in the crack region, and (c) Maximum principal stress before void initiation.

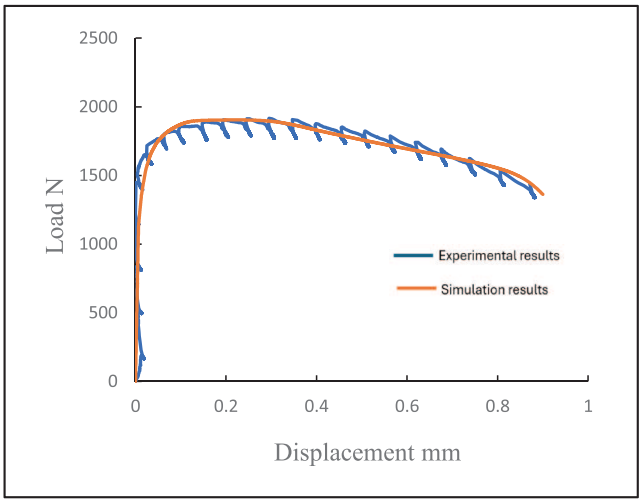

Fig. 17. Simulation results of the best adjustment curve for GTN parameters compared with experimental results.

calibration approach. These differences highlight the importance of geometry-specific calibration for improving the predictive accuracy of the GTN model, particularly when simulating microscale experiments such as in-situ SEM tensile tests.

In the context of fracture analysis, it is essential to clearly define the stress and strain components discussed. In this work, the analysis focuses on maximum principal stress, maximum principal strain, and stress triaxiality, as these parameters are directly related to fracture initiation in ductile metals. The maximum principal stress identifies critical tensile regions prone to crack initiation (Figs. 5 and 17), while the maximum principal strain highlights zones of large plastic deformation. Stress triaxiality, representing the ratio of mean stress to equivalent von Mises stress, is a key factor in controlling void growth rates and is directly embedded in the GTN formulation.

Figs. 5 and 17 illustrate that regions exhibiting elevated maximum principal stress and strain, combined with high stress triaxiality, coincide with experimentally observed fracture initiation sites (Figs. 5 and 17). This correlation confirms that the GTN model does not merely fit the global load–displacement curve but also captures the local stress–-strain state leading to fracture, validating its physical significance.

3.2. *In-situ bending behaviour and microstructural evolution in Dual-Phase steel*

To overcome the limitations of the SEM tensile test, a three-point bending setup was employed using a custom specimen geometry (Fig. 2) designed to promote surface cracking for SEM observation (Fig. 18). The test was interrupted every 0.25 mm to capture SEM images for DIC-based strain analysis.

(i) Localized Plastic Deformation

Fig. 18 presents a low-magnification view showing surface cracks under maximum tensile stress. A localized region (blue rectangle) was analysed to study damage development relative to strain distribution. The initial image (Fig. 18(o)) highlights the undeformed region where deformation bands later appeared. At 1.5 mm displacement (Fig. 18 (a)), early ferrite deformation was observed (blue circles), with two deformation bands forming (oval red shapes), initiated at the locations marked by the black arrow. As displacement increased to 1.75 mm (Fig. 18 (b)), deformation became more localized, indicating the onset of damage. Final deformation before fracture is shown in Fig. 18 (c).

In both tensile and bending tests, plastic deformation in DP1000 steel initiated primarily in the ferrite phase due to its higher ductility. However, in the tensile test, strain localisation developed early and more uniformly across the gauge section, forming distinct 45° deformation bands. In contrast, the bending test showed strain localisation confined

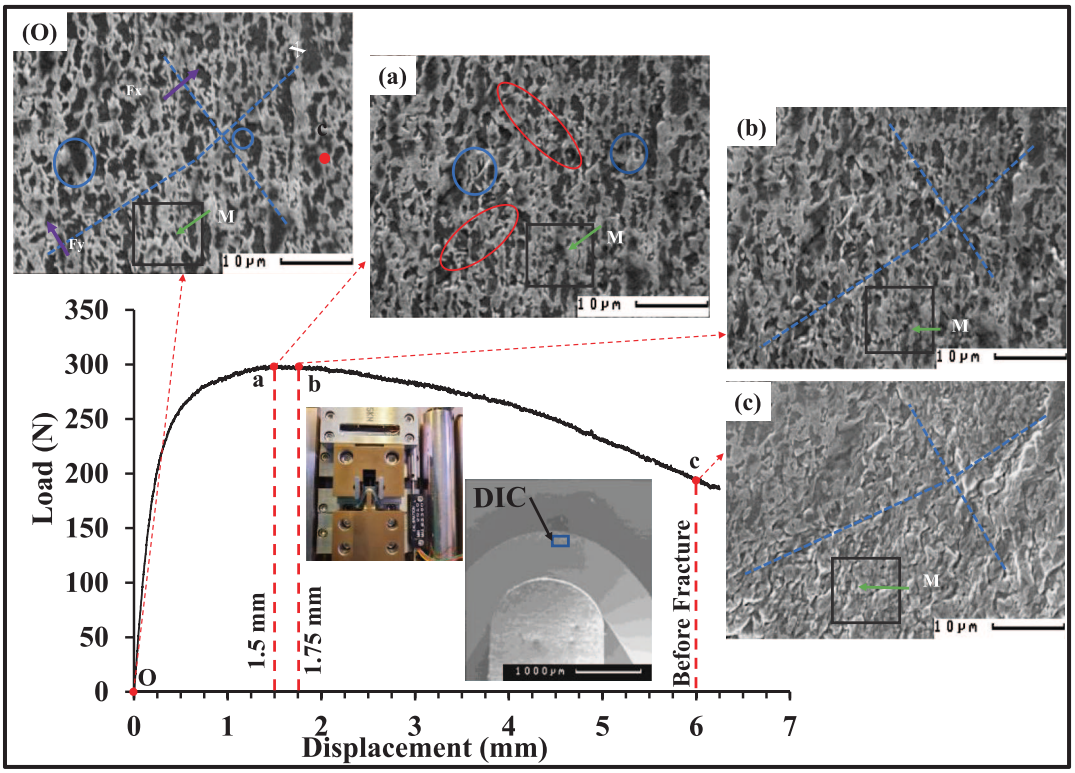

Fig. 18. In-situ Bending test (o) No load expected deformation of lines X and Y, (a) Initial deformation of both lines (black and red arrows), early deformation in the ferrite phase (blue rectangle and circles) and the continuation of deformation (black squares), (b) Continuation of deformation mechanism, (c) Stage before final fracture. (For interpretation of the references to colour in this figure legend, the reader is referred to the web version of this article.)

near the tensile surface, driven by the through-thickness stress gradient. While tensile loading led to widespread damage and higher peak local strain values (up to 2.5), the bending test exhibited more surface-focused damage, with deformation bands forming later and progressing more gradually. Despite these differences, both tests confirmed that ferrite–martensite interfaces are critical zones for crack initiation.

(ii) Inspection of martensite cracks and ferrite voids.

Analysis of the bending test revealed the formation of martensite cracks at multiple locations within the region studied using Digital Image Correlation (DIC). These cracks likely originated either from severe plastic deformation of the surrounding ferrite or directly within the martensite due to localized stress concentration. The sequence of martensite cracking during ductile bending, along with the corresponding load-extension behaviour, is illustrated in Fig. 19.

The first crack (Crack 1) appeared at a displacement of 1.25 mm, where a martensite region cleaved into two segments before reaching the peak load of 295 N (Fig. 19 (a)). This initial fracture was followed by Cracks 2 and 3, which were triggered by localized plastic deformation in the ferrite adjacent to martensite. Crack 2 initiated at 1.75 mm under a load of 298 N, while Crack 3 occurred at 2.0 mm and 297 N (Fig. 19 (b) and (c)), indicating that strain localization in ferrite contributed to the subsequent failure of martensite. As deformation progressed, Crack 4 emerged at 2.25 mm and 294 N. This event was characterized by the coalescence of two deformed ferrite regions near a previously fractured martensite zone, forming a new microcrack (Fig. 19 (d)). Subsequently, Crack 5 developed at the maximum extension of 2.5 mm under a load of 292 N. It resulted from the propagation of a microcrack, initially formed in the ferrite, which extended into the martensite and caused its failure (Fig. 19 (e)). Finally, Crack 6 occurred beyond the peak load, at a displacement of 3.0 mm and a reduced load of 285 N. Like the previous event, it originated as a microcrack in the ferrite and propagated into the martensite (Fig. 19 (f)). Collectively, these observations emphasize the progressive nature of damage evolution under bending and highlight the coupled role of ferrite plasticity and martensite fracture in crack initiation and growth.

(iii) DIC Analysis: Strain Distribution

The damage evolution and local deformation behaviour observed during the bending test were further evaluated using DIC. Strain distribution was calculated in the Y-direction, which corresponds to the tensile axis in the bending specimen. This section presents the spatial development of strain across the microstructure. Fig. 20 (a) shows the strain distribution map at a displacement of 1.5 mm. At this stage, the maximum localized strain of approximately 0.32 was observed in the ferrite phase, as indicated by the arrows. In contrast, the martensite islands exhibited significantly lower strain, consistent with their higher strength and lower ductility. As deformation progressed to 1.75 mm, strain localization became more pronounced, particularly in groups of microstructures as shown in Fig. 20 (b). The arrows highlight two distinct lines of elevated strain values, where martensite cracking and ferrite void formation were expected to occur, correlating with the fracture events discussed earlier (see Fig. 19).

The peak strain further intensified in the ferrite phase, eventually reaching up to 1.3 just before damage initiation. Fig. 20 (c) presents the strain map at a displacement of 5.5 mm, immediately before final fracture. Throughout the test, localized strain remained concentrated in specific ferrite regions, indicating persistent deformation in these zones. Notably, E_{YY}, the Lagrangian strain component along the Y-axis (vertical in the images), clearly shows how strain accumulated in ferrite areas. This strongly suggests that ferrite plays a dominant role in accommodating plastic strain and initiating damage. The results confirm that high strain localization originated in the ferrite phase and progressed until final fracture. Consequently, ferrite is likely the controlling phase in damage evolution for DP1000 steel under bending.

(iv) DIC Analysis: Martensite Microcracking and Ferrite Void Nucleation

To complement the strain distribution analysis from DIC and the fracture sequence discussed earlier, high-magnification SEM imaging was conducted during the bending tests to gain detailed insight into the formation of martensite cracks and ferrite voids. These observations are summarized in Fig. 21, which illustrates local strain distributions at the onset of martensite cracking for cracks 1 through 6. Cracks 1, 2, and 3 were initiated at local strain values of 0.21, 0.225, and 0.2, respectively (see Fig. 21 (a)–(c)). These strain levels correspond closely with the high localised strain regions in the ferrite phase identified earlier in the DIC

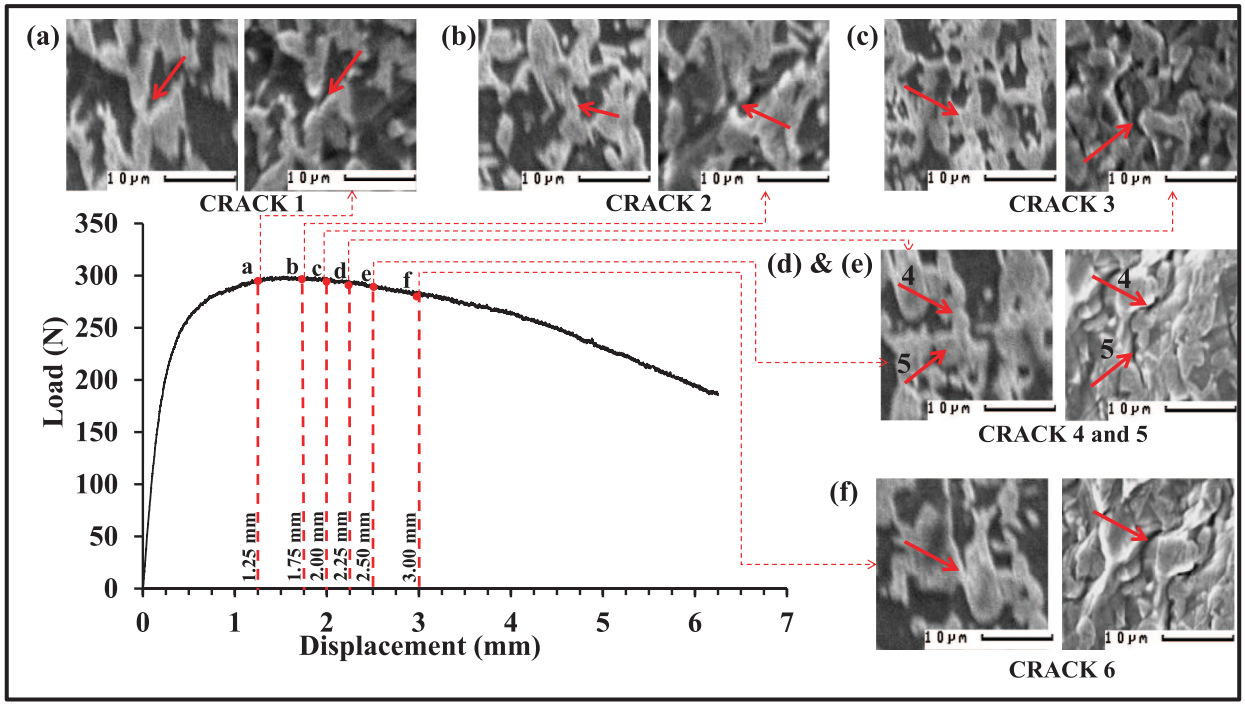

Fig. 19. Martensite cracks mechanism at different displacement values (a) 1.25 mm (crack 1), (b) 1.75 mm (crack 2), (c) 2.00 mm (crack 3), (d) 2.25 mm (crack 4), (e) 2.50 mm (crack 5), and (f) 3.00 mm (crack 6).

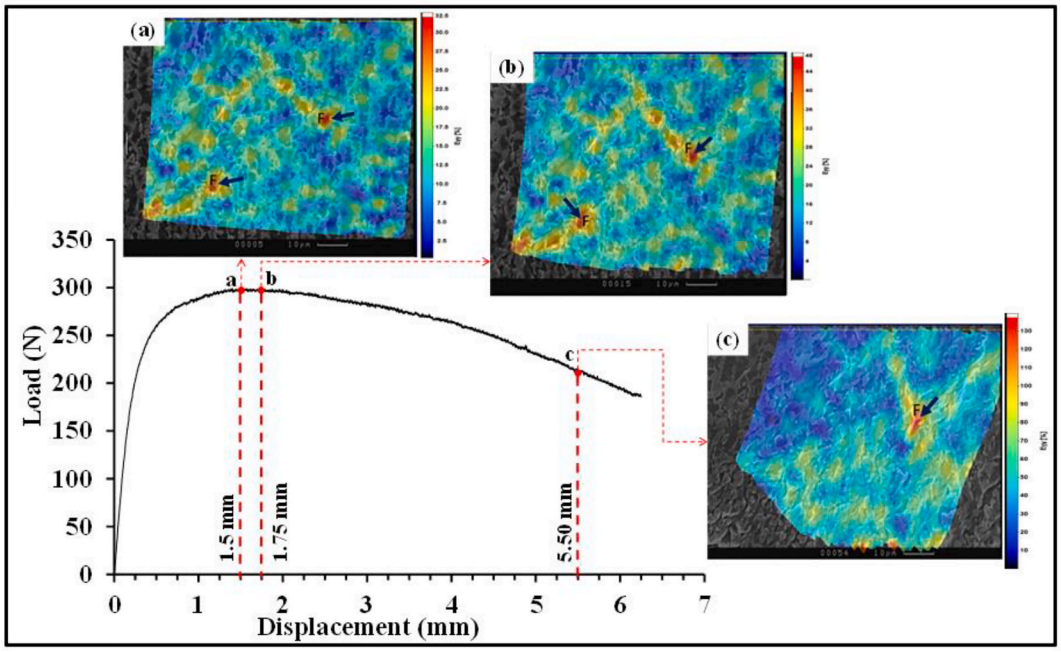

Fig. 20. In-situ Bending Test DIC analysis at different displacement values (a) 1.5 mm, (b) 1.75 mm, and (c) 5.5 mm.

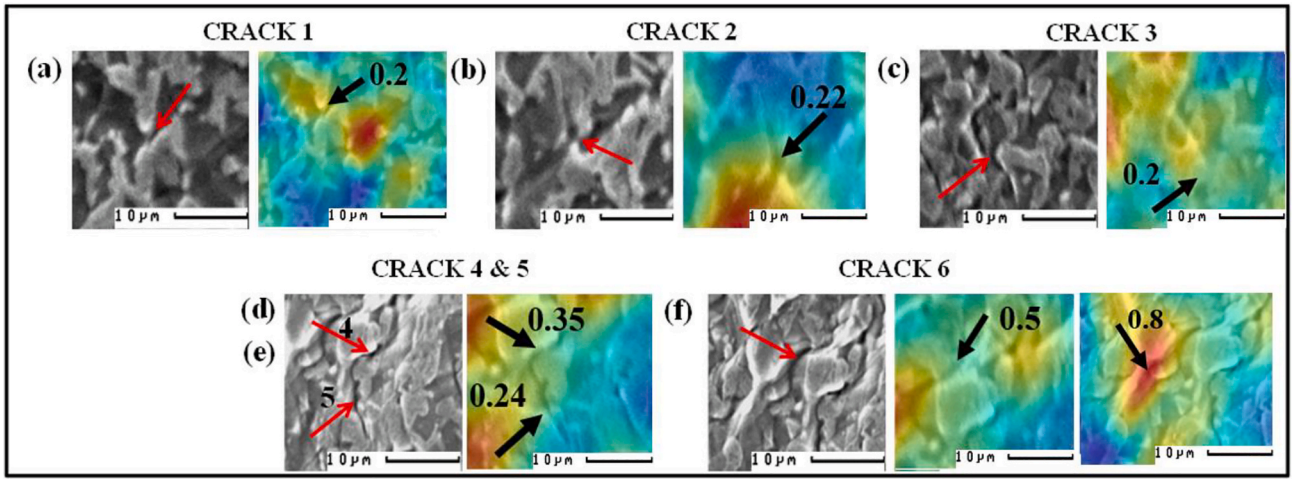

Fig. 21. Strain distributions to the onset of the martensite cracking (a) Crack 1, (b) Crack 2, (c) Crack 3, (d) Crack 4, (e) Crack 5, and (f) Crack 6.

strain maps (Fig. 20), supporting the conclusion that ferrite deformation precedes and promotes martensite fracture. Crack 4, which occurred at a higher local strain value of 0.35 Ɛ (Fig. 21 (d)), resulted from the coalescence of strain within two neighbouring ferrite zones. Interestingly, although crack 5 appeared at a higher global displacement, it formed under a lower local strain of 0.24 (Fig. 21 (e)), indicating the influence of localized microstructural features on crack propagation.

Crack 6 (Fig. 21 (f)) likely initiated in the martensite under the influence of a nearby microcrack in ferrite, where the local strain had reached a peak of 0.8. This is consistent with prior observations that localized strain in the ferrite phase accumulates and transfers stress to the adjacent martensite, eventually causing fracture. The accumulation of strain within ferrite regions plays a key role in triggering subsequent martensite cracking and overall failure under bending.

4. Discussion

4.1. Plastic deformation and GTN model

The mechanical response of DP1000 steel is characterized by a high UTS of 1070 MPa and a notable strain to failure of 0.36, as evidenced by the SEM-based tensile results shown in Fig. 5. In-situ tensile testing revealed substantial plastic deformation occurring at the microstructural level. As illustrated in Fig. 7, localized strain values reached up to 2.5 in the ferrite phase and 2.2 in martensite before failure. These exceptionally high strain levels align well with prior studies by Ghadbeigi et al. [18] and Rohaizat [63], corroborating the significant ductility exhibited by the martensite phase in DP1000—a feature that distinguishes this dual-phase steel from traditional high-strength steels. Complementary results from the in-situ SEM bending tests further confirmed high levels of plasticity within both phases, with maximum local strain values around 1.35 in ferrite and 0.90 in martensite (see Fig. 14). At the UTS point in the tensile test, the strain distribution map

(refer Fig. 8) displayed mean strain values of approximately 0.10 in both phases, again consistent with Rohaizat's [63] findings.

Importantly, regardless of the testing geometry (tensile or bending), plastic deformation in DP1000 initiates within the ferrite phase. This is first evidenced by the emergence of localized deformation bands, as shown in Figs. 5 and 18, respectively. As loading continues, these bands expand and interconnect across ferrite-rich regions, concentrating strain and forming preferential pathways for damage evolution (Figs. 7 and 20, respectively). With increasing deformation, the concentrated plasticity in ferrite transmits stress to the adjoining martensite islands, leading to their eventual cracking or fracture. This progression confirms that while martensite plays a critical role in strengthening, the ferrite matrix governs the initiation and evolution of plastic deformation in DP1000.

The GTN model, which is commonly used to simulate the damage of ductile materials, was also applied to DP steels in the literature [27,30,61]. The GTN model was therefore selected for this work as it had been successfully applied to DP1000 previously [27]. Calibration of the damage parameters is commonly performed using an SEM specimen. From Table 5 and Fig. 17 model can provide a very good match with the experimental curves by adjusting the model parameters $S_n, f_n, \epsilon_n, q_1$, q_2, and q_3. The validity of the damage model is assessed by comparing experimental load displacement curves with those obtained from model predictions, as reported in [25,26]. In the current investigation, the model was successfully validated against the load–displacement curve recorded during the in-situ tensile test with a specimen geometry designed to highly concentrate stresses in a very small gauge length to facilitate damage observations in the SEM, while ensuring compatibility with the maximum load capacity of the in-situ tensile stage.

4.2. Martensitic cracking and damage initiation

In-situ tensile and bending test results on DP1000 show that damage initiates at the microstructural level, typically beginning with martensite cracking near the UTS in tensile tests (Fig. 11) and at peak load during bending (Fig. 19). While martensite cracking can continue beyond these points, it is most frequent around the maximum force. Three main mechanisms were identified: (1) martensite cracking without notable ferrite deformation; (2) cracking preceded by significant strain in ferrite; and (3) cracking triggered by nearby ferrite void formation (refer to Figs. 6 and 19, respectively). These mechanisms confirm martensite cracking as an early damage mode in DP1000, consistent with Alharbi [15,27,55] and Ghadbeigi et al. [18]. In addition, prior austenite grain boundaries (PAGBs) may influence martensite cracking indirectly by facilitating void nucleation in the surrounding ferrite phase. These boundaries can act as sites of local strain concentration and microstructural incompatibility, leading to accelerated damage accumulation. The proximity of such voids to ferrite–martensite interfaces increases the likelihood of stress-driven martensite cracking. It is also recognized that crack propagation observed in the later stages of deformation includes contributions from coalesced voids, particularly within heavily deformed ferrite zones. This reinforces the transition from microvoid nucleation to crack formation as a continuum in ductile fracture behavior. DIC analysis revealed that martensite cracks initiated at local strain values ranging from 0.088 % to 1.43 in tensile tests and 0.20 to 0.50 in bending, with most occurring between 0.15 and 0.45 (Figs. 9 and 21, respectively). These values show a broader distribution than those reported in Rohaizat [63] due to variations in material heat treatments and larger sample sizes in this study. Finite three-dimensional finite element analysis (FEA) of representative volume elements (RVEs) representing dual-phase (DP) steel microstructures demonstrated that martensite morphology strongly governs strain distribution, tensile strength, and damage evolution [24]. Integrating the experimental results into FE simulations to estimate stress states in regions that are difficult to measure directly has been demonstrated in [22,25,26]. In this work, the finite element simulations supported a stress-driven mechanism, with cracks initiating at principal stresses around 1783 MPa, aligning with Alharbi et al. [27]. However, not all high-stress martensite regions cracked, suggesting that both stress and local microstructural context influence damage. Overall, martensite cracking is the earliest damage event but does not directly lead to failure. Cracks arrest at ferrite interfaces, and the final fracture is driven by extensive deformation and voiding in ferrite (Fig. 7), emphasizing ferrite's dominant role in controlling fracture in DP1000.

4.3. Void nucleation in the ferrite phase

This study provides a detailed investigation into void nucleation within the ferrite phase of DP1000 steel during in-situ tensile testing, marking one of the first systematic reports of multiple void initiation events in ferrite. Voids were predominantly observed near the end of the test, close to the final fracture, which explains their limited presence in conventional studies that focus on earlier stages of deformation. Previous works, such as Ghadbeigi et al. [18], reported only a single occurrence of void formation. DIC revealed that voids nucleated at local strain levels between 0.75 and 1.40, in line with the 1.20 strain value from Ghadbeigi et al. [18] and ductile damage models. FE analysis showed that voids formed in regions with local stresses ranging from 915–990 MPa, although not at the highest stress points. A void observed within a ferrite region constrained by martensite highlights the role of microstructural constraints in damage localization (Fig. 16). These results indicate that void nucleation in ferrite is primarily strain-driven, occurring after significant plastic deformation. However, void growth and coalescence could not be observed before specimen fracture [64].

4.4. Damage propagation

To investigate damage development in DP1000 steel, large crack growth was analysed using in-situ SEM bending tests on two specimens. The first was used for local strain analysis via DIC [10,11,17,18,26,27,62], while the second allowed full tracing of crack initiation and progression. In both tests, cracks were observed to initiate at the specimen edge, where maximum tensile stress arises during bending, and then propagate significantly across the surface. One example shown in Fig. 22 (a) – (c) crack propagation of 0.0168 mm before changing direction by 0.006 mm, with nearby void formation and microcracks indicating early damage accumulation in ferrite. The in-situ tensile test underscored limitations in capturing subsurface damage, as failure often initiates at mid-thickness and propagates toward the surface, making surface-level tracking difficult. To overcome this, a bespoke specimen geometry with a slanted top surface (Fig. 2) was designed. This configuration successfully facilitated surface crack initiation and propagation, allowing observation of damage mechanisms in the SEM.

A representative case (Fig. 20) confirmed that cracks initiated in ferrite, then interacted with local martensite clusters, which acted as obstacles, inducing significant plastic deformation ahead of the crack tip. As deformation increased, secondary cracks formed in the surrounding ferrite and coalesced with the main crack. In both specimens, crack paths initially followed shear-dominated trajectories (~45° to the loading axis) and were later deflected by microstructural heterogeneities. One tracked crack propagated 0.446 mm at 45°, followed by 0.068 mm after reorienting (Fig. 22 (d) and (e)). This behaviour highlights the influence of stress redistribution and phase interactions on crack evolution. The second bending test enabled stepwise tracking of damage development from nucleation in ferrite to coalescence and eventual fracture, demonstrating the effectiveness of the custom geometry in capturing crack growth dynamics in dual-phase steels.

5. Conclusion

This study comprehensively explored the damage initiation and propagation mechanisms in DP1000 steel using in-situ SEM-based

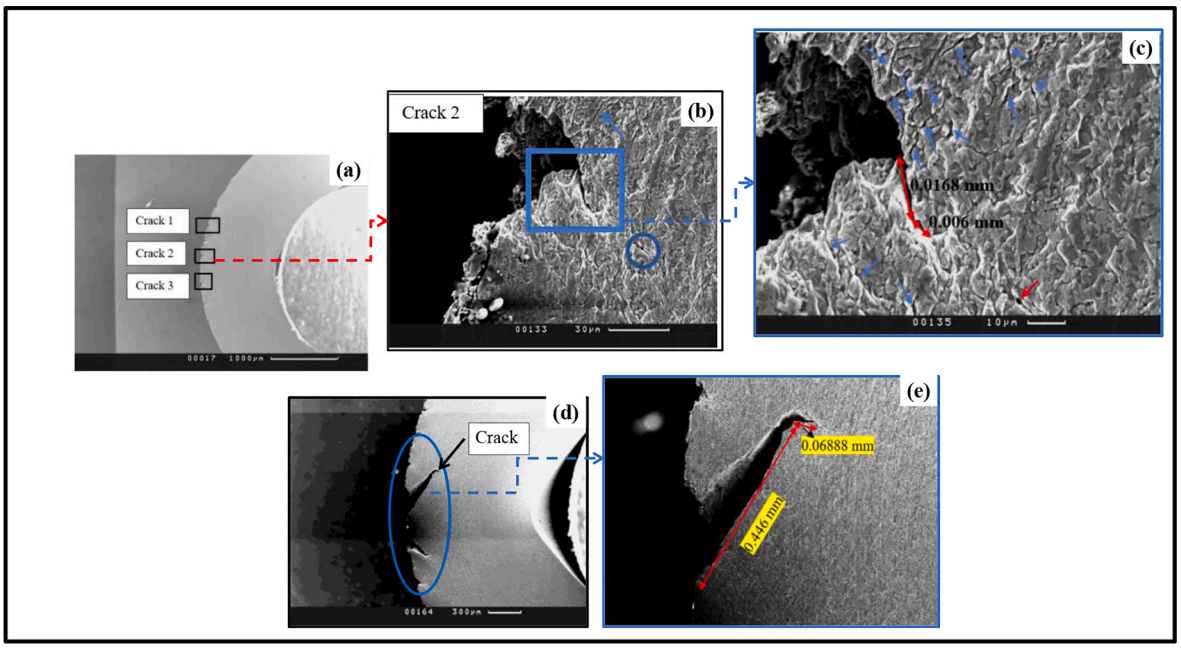

Fig. 22. Crack propagation and damage with higher magnification (a & d) Cracks at different magnification, (b) Crack 2 magnification, (c) Crack propagation before changing direction, (e) Crack propagated 0.446 mm at 45° and 0.068 mm after reorientation.

tensile and bending tests, complemented by DIC and FE analysis. The experimental approach provided high-resolution insights into local deformation and damage evolution in both martensite and ferrite phases, revealing the intricate relationship between microstructural heterogeneity and local stress–strain states that influence phase-specific damage behaviour and crack development. Some of the key findings from this study are as follows:

- *Plastic Deformation Initiation:* Plastic deformation in DP1000 steel primarily initiates in the ferrite phase, with local strain values reaching up to 2.50 in ferrite and 2.20 in martensite during tensile loading. This highlights the high ductility of both phases and emphasizes the dominant role of ferrite in the deformation evolution process.
- *Martensite Cracking:* Cracking in martensite primarily occurs at ferrite–martensite interfaces under localized strain, with initiation observed at strain levels between 0.088 and 1.43 in tension and 0.20 to 0.50 in bending tests. These cracks serve as critical sites for further damage evolution.
- *Void Nucleation in Ferrite:* Voids in ferrite nucleate primarily under high local strain (0.75–1.40) and moderate local stresses (915–990 MPa), usually near fracture. Microstructural constraints, such as surrounding martensite islands, significantly influence the localization of damage and void formation.
- *FE Analysis Confirmation:* The FE simulations using the GTN damage model results are closely aligned with the experimental findings, confirming that void nucleation in ferrite occurs in regions with local stresses of 915–990 MPa. This further substantiates the strain-driven nature of void formation, influenced by microstructural features.
- *Crack Propagation Mechanisms:* In-situ SEM tests with a custom specimen geometry revealed that cracks initiate in the ferrite phase, propagate through martensite islands, and follow shear-dominated paths (~45° to the loading axis). This crack propagation is accompanied by significant plastic deformation and secondary crack formation, which highlights the role of microstructural heterogeneities and stress redistribution in crack evolution.

The integration of experimental techniques and modelling provided a comprehensive understanding of the damage mechanisms in DP1000, offering critical insights that are essential for improving the design and performance of advanced high-strength steels. These findings lay the foundation for the development of more accurate damage models and the optimization of alloy compositions for future applications.

CRediT authorship contribution statement

Asim Alsharif: Writing – original draft, Visualization, Project administration, Methodology, Investigation, Funding acquisition, Formal analysis, Conceptualization. **Syed Quadir Moinuddin:** Writing – review & editing, Writing – original draft, Validation, Project administration, Investigation, Funding acquisition, Data curation. **R. Dowding:** Writing – review & editing, Visualization, Supervision, Software, Resources, Investigation, Conceptualization. **C. Pinna:** Writing – review & editing, Visualization, Validation, Supervision, Resources, Methodology, Investigation, Conceptualization.

Funding

This work was supported by Taibah University, Medinah, Saudi Arabia.

This work was supported by the Deanship of Scientific Research, Vice Presidency for Graduate Studies and Scientific Research, King Faisal University, Saudi Arabia [Grant No. KFU251869].

Declaration of competing interest

The authors declare that they have no known competing financial interests or personal relationships that could have appeared to influence the work reported in this paper.

Acknowledgments

The authors are grateful to Tata Steel Europe, IJmuiden, the Netherlands, for providing the material for this research. Furthermore, the first and second authors would like to express their sincere gratitude to Taibah University and the Deanship of Scientific Research, King Faisal University, Saudi Arabia [Grant No. KFU251869], for their generous financial support, which was essential in making this research possible.

Data availability

The experimental datasets obtained from this research work and then the analysed results during the current study are available from the corresponding author on reasonable request.

References

[1] C.C. Tasan, J.P.M. Hoefnagels, M. Diehl, D. Yan, F. Roters, D. Raabe, Strain localization and damage in dual phase steels investigated by coupled in-situ deformation experiments and crystal plasticity simulations, Int. J. Plast 63 (2014) 198–210, https://doi.org/10.1016/j.ijplas.2014.06.004.

[2] S.J. Song, W.K. Che, J.B. Zhang, L.K. Huang, S.Y. Duan, F. Liu, Kinetics and microstructural modeling of isothermal austenite-to-ferrite transformation in Fe-C-Mn-Si steels, J. Mater. Sci. Technol. 35 (2019) 1753–1766, https://doi.org/10.1016/j.jmst.2019.04.010.

[3] E. De Moor, Advanced high-strength sheet steels for automotive applications, in: R. Rana (Ed.), High-Performance Ferrous Alloys, Springer International Publishing, 2020, pp. 113–151, https://doi.org/10.1007/978-3-030-53825-5_4.

[4] D. Ivkovic, D. Adamovic, D. Arsić, N. Ratkovic, A. Mitrović, R. Nikolic, Review of the advanced high-strength steels used in automotive industry, Mobility Veh. Mech. 3 (2024) 47–64. https://doi.org/10.24874/mvm.2023.48.03.04.

[5] D.K. Matlock, J.G. Speer, Third generation of AHSS: microstructure design concepts, AIST Trans. 1 (2009) 1–7, https://doi.org/10.1007/978-1-84882-454-6_11.

[6] G. Rosenberg, I. Sinaiová, Ľ. Juhar, Effect of microstructure on mechanical properties of dual phase steels in the presence of stress concentrators, Mater. Sci. Eng. A 582 (2013) 347–358, https://doi.org/10.1016/j.msea.2013.06.035.

[7] M. Tisza Three generations of advanced high strength steels in the automotive industry K. Jármai K. Voith Vehicle and Automotive Engineering 3 Lecture Notes in Mechanical Engineering 2021 Springer, Singapore 81 94 10.1007/978-981-15-9529-5_7.

[8] R.O. Santos, L.P. Moreira, M.C. Butuc, G. Vincze, A.B. Pereira, Damage analysis of third-generation advanced high-strength steel based on the Gurson–Tvergaard–Needleman (GTN) model, Metals 12 (2022) 214, https://doi.org/10.3390/met12020214.

[9] J. Kang, M. Jain, D.S. Wilkinson, J.D. Embury, Microscopic strain mapping using scanning electron microscopy topography image correlation at large strain, J. Strain Anal. Eng. Des. 40 (2005) 559–570, https://doi.org/10.1243/030932405X16151.

[10] J. Kang, Y. Ososkov, J.D. Embury, H.S. Zurob, Digital image correlation studies for microscopic strain distribution and damage in dual phase steels, Scr. Mater. 56 (2007) 999–1002, https://doi.org/10.1016/j.scriptamat.2007.01.031.

[11] Y. Ososkov, J. Kang, J.D. Embury, H.S. Zurob, In-situ measurement of local strain partitioning in a commercial dual-phase steel, Int. J. Mater. Res. 98 (2007) 664–673, https://doi.org/10.3139/146.101526.

[12] X. Sun, K.S. Choi, W.N. Liu, M.A. Khaleel, Predicting failure modes and ductility of dual phase steels using plastic strain localization, Int. J. Plast 25 (2009) 1888–1909, https://doi.org/10.1016/j.ijplas.2008.12.012.

[13] A.C. Darabi, V. Guski, A. Butz, J. Kadkhodapour, S. Schmauder, A comparative study on mechanical behavior and damage scenario of DP600 and DP980 steels, Mech. Mater. 143 (2020) 103339, https://doi.org/10.1016/j.mechmat.2020.103339.

[14] M. Calcagnotto, D. Ponge, E. Demir, D. Raabe, Orientation gradients and geometrically necessary dislocations in ultrafine-grained dual-phase steels studied by 2D and 3D EBSD, Mater. Sci. Eng. A 527 (2011) 2738–2746, https://doi.org/10.1016/j.msea.2010.01.004.

[15] H.F. Alharbi, D.S. Wilkinson, M.K. Jain, Micromechanical damage modeling in DP1000 steel using in-situ SEM tensile testing and FE simulations, Int. J. Mech. Sci. 101–102 (2015) 465–475. https://doi.org/ 10.1088/0965-0393/23/8/085005.

[16] B. Marrapu, V.K. Barnwal, S. Chakrabarty, et al., Experimental and numerical analysis on dual phase steel (DP780) sheet forming limit and effect of microstructure evolution on formability, J. Mater. Eng. Perform. 29 (2020) 8247–8260, https://doi.org/10.1007/s11665-020-05247-1.

[17] G. Avramovic-Cingara, Y. Ososkov, M.K. Jain, D.S. Wilkinson, Effect of martensite distribution on damage behaviour in DP600 dual phase steels, Mater. Sci. Eng. A 516 (2009) 7–16, https://doi.org/10.1016/j.msea.2009.03.055.

[18] H. Ghadbeigi, C. Pinna, S. Celotto, J.R. Yates, Local plastic strain evolution in a dual-phase steel, Mater. Sci. Eng. A 527 (2010) 5026–5032, https://doi.org/10.1016/j.msea.2010.04.052.

[19] N. Saeidi, F. Ashrafizadeh, B. Niroumand, Development of a new ultrafine grained dual phase steel and examination of the effect of grain size on tensile deformation behavior, Mater. Sci. Eng. A 599 (2014) 145–149, https://doi.org/10.1016/j.msea.2014.01.053.

[20] M. Erdoğan, The effect of new ferrite content on the tensile fracture behaviour of dual phase steels, J. Mater. Sci. 37 (2002) 3623–3630, https://doi.org/10.1023/A:1016548922555.

[21] H. Ghadbeigi, C. Pinna, S. Celotto, Failure mechanisms in DP600 steel: initiation, evolution and fracture, Mater. Sci. Eng. A 588 (2013) 420–431, https://doi.org/10.1016/j.msea.2013.09.048.

[22] J. Kadkhodapour, A. Butz, S.Z. Rad, Mechanisms of void formation during tensile testing in a commercial, dual-phase steel, Acta Mater. 59 (2011) 2575–2588, https://doi.org/10.1016/j.actamat.2010.12.039.

[23] A. Alaie, N. Aravas, J.W. Yoon, Effect of microstructure pattern on the strain localization in DP600 steels analyzed using combined in-situ experimental test and numerical simulation, Mater. Sci. Eng. A 638 (2015) 251–261, https://doi.org/10.1016/j.msea.2015.04.071.

[24] T. Matsuno, T. Yoshioka, I. Watanabe, L. Alves, Three-dimensional finite element analysis of representative volume elements for characterizing the effects of martensite elongation and banding on tensile strength of ferrite-martensite dual-phase steels, Int. J. Mech. Sci. 163 (2019) 105133, https://doi.org/10.1016/j.ijmecsci.2019.105133.

[25] M. Ohata, M. Toyoda, Damage concept for evaluating ductile cracking of steel structure subjected to large-scale cyclic straining, Sci. Technol. Adv. Mater. 5 (2004) 241–249, https://doi.org/10.1016/j.stam.2003.10.007.

[26] G.H. Gu, J. Kwon, J. Moon, H. Kwon, J. Lee, Y. Kim, E.S. Kim, M.H. Seo, H. Hwang, H.S. Kim, Determination of damage model parameters using nano- and bulk-scale digital image correlation and the finite element method, J. Mater. Res. Technol. 17 (2022) 392–403, https://doi.org/10.1016/j.jmrt.2022.01.012.

[27] K. Alharbi, D.S. Wilkinson, M.K. Jain, Damage in dual phase steel DP1000 investigated using digital image correlation and microstructure simulation, Model. Simul. Mater. Sci. Eng. 23 (2015) 085005, https://doi.org/10.1088/0965-0393/23/8/085005.

[28] A.L. Gurson, Continuum theory of ductile rupture by void nucleation and growth: Part I—Yield criteria and flow rules for porous ductile media, J. Eng. Mater. Technol. 99 (1977) 2–15, https://doi.org/10.1115/1.3443401.

[29] V. Tvergaard, Influence of voids on shear band instabilities under plane strain conditions, Int. J. Fract. 17 (1981) 389–407, https://doi.org/10.1007/BF00036191.

[30] V. Tvergaard, On localization in ductile materials containing spherical voids, Int. J. Fract. 18 (1982) 237–252, https://doi.org/10.1007/BF00015686.

[31] V. Tvergaard, Material failure by void growth to coalescence, Adv. Appl. Mech. 27 (1989) 83–151, https://doi.org/10.1016/S0065-2156(08)70195-9.

[32] S. Qin, Y. Lu, S.B. Sinnott, A.M. Beese, Influence of phase and interface properties on the stress state dependent fracture initiation behavior in DP steels through computational modeling, Mater. Sci. Eng. A 776 (2020) 138981, https://doi.org/10.1016/j.msea.2020.138981.

[33] J. Kim, X. Gao, T.S. Srivatsan, Modeling of void growth in ductile solids: effects of stress triaxiality and initial porosity, Eng. Fract. Mech. 71 (3) (2004) 379–400, https://doi.org/10.1016/S0013-7944(03)00114-0.

[34] T. Zhang, J.H. Kim, M.G. Lee, A hybrid experimental–numerical framework to characterize fracture behaviors in DP steels, Mater. Des. 197 (2021) 109253, https://doi.org/10.1016/j.ijsolstr.2009.12.011.

[35] M. Abbasi, A. Assempour, A. Ghaei, H.R. Barzegari, Identification of GTN model parameters by application of response surface methodology, Procedia Eng. 10 (2011) 415–420, https://doi.org/10.1016/j.proeng.2011.04.070.

[36] W. Wcislik, Experimental determination of critical void volume fraction for the Gurson–Tvergaard–Needleman (GTN) model, Procedia Struct. Integr. 2 (2016) 1676–1683, https://doi.org/10.1016/j.prostr.2016.06.212.

[37] K. Nahshon, J.W. Hutchinson, Modification of the Gurson model for shear failure, Eur. J. Mech. A Solids 27 (1) (2008) 1–17, https://doi.org/10.1016/j.euromechsol.2007.08.002.

[38] N.H. Abid, R.K.A. Al-Rub, A.N. Palazotto, Computational modeling of the effect of equiaxed heterogeneous microstructures on strength and ductility of dual phase steels, Comput. Mater. Sci 103 (2015) 20–37, https://doi.org/10.1016/j.commatsci.2015.02.051.

[39] S.K. Paul, Micromechanics based modeling of dual phase steels: Prediction of ductility and failure modes, Comput. Mater. Sci 56 (2012) 34–42, https://doi.org/10.1016/j.commatsci.2011.12.031.

[40] H. Hosseini-Toudeshky, M. Mohammadzadeh, M.H. Abolbashari, Microstructural deformation pattern and mechanical behavior analyses of DP600 dual phase steel, Mater. Sci. Eng. A 600 (2014) 108–121, https://doi.org/10.1016/j.msea.2014.02.016.

[41] R. Dowding, R. Mishra, I. Charit, T.W. Lim, J. Bains, Analyzing the properties promoting shear bands and damage initiation in 3-point bending of ultra-high strength steel, Procedia Manuf. 50 (2020) 570–573, https://doi.org/10.1016/j.promfg.2020.08.102.

[42] M.A. Sutton J.J. Orteu H. Schreier . First, Image Correlation for Shape, Motion and Deformation Measurements: Basic Concepts, Theory and Applications 2009 Springer New York 10.1007/978-0-387-78747-3.

[43] H. Ghadbeigi, C. Pinna, S. Celotto, Quantitative strain analysis of the large deformation at the scale of microstructure: comparison between digital image correlation and microgrid techniques, Exp. Mech. 52 (2012) 1483–1492, https://doi.org/10.1007/s11340-012-9612-6.

[44] ABAQUS Dassault, Systèmes 6.10/CAE User's Manual, Dassault Systèmes Simulia Corp, Providence .

[45] T.A. Davis, MATLAB Primer, 7th ed., CRC Press, Boca Raton, 2010.

[46] I. Chalon, Modelling of the microstructural deformation of duplex stainless steel during plane strain compression, The University of Sheffield, Sheffield, 2004. PhD Thesis.

[47] T. Sirinakorn, V. Uthaisangsuk, Investigation of damage initiation in high-strength dual-phase steels using cohesive zone model, Int. J. Damage Mech 27 (3) (2018) 409–438, https://doi.org/10.1177/1056789516679718.

[48] E. Maire, J. Adrien, O. Bouaziz, Initiation and growth of damage in a dual-phase steel observed by X-ray microtomography, Acta Mater. 56 (18) (2008) 4954–4964, https://doi.org/10.1016/j.actamat.2008.06.015.

[49] F. Pütz, J. Nitzsche, T. Hama, P. Hähner, M. Kuna, The differences of damage initiation and accumulation of DP steels: a numerical and experimental analysis, Int. J. Fract. 226 (2020) 1–15, https://doi.org/10.1007/s10704-020-00457-z.

[50] C. Tian, N. Jia, X. Sun, T. Park, L. Luo, Understanding the damage initiation and growth mechanisms of two DP800 dual phase grades, Mater. Des. 238 (2024) 112630, https://doi.org/10.1016/j.matdes.2024.112630.
[51] S. Nemat-Nasser, M. Hori, Micromechanics: overall Properties of Heterogeneous Materials, 2nd ed., Elsevier, Amsterdam, 1999.
[52] S.A. Asgari, P.D. Hodgson, C. Yang, B.F. Rolfe, Modeling of advanced high strength steels with the realistic microstructure–strength relationships, Comput. Mater. Sci 45 (2009) 860–866, https://doi.org/10.1016/j.commatsci.2008.12.003.
[53] G. Avramovic-Cingara, C.A.R. Saleh, M.K. Jain, D.S. Wilkinson, Void nucleation and growth in dual-phase steel 600 during uniaxial tensile testing, Metall. Mater. Trans. A 40 (2009) 3117–3127, https://doi.org/10.1007/s11661-009-0030-z.
[54] J. Besson, Continuum models of ductile fracture: a review, Int. J. Damage Mech 18 (2009) 527–561, https://doi.org/10.1177/1056789509103482.
[55] K. Alharbi, Damage investigation in dual-phase 1000 steel and behaviour prediction using microstructure based modelling, University of Sheffield, 2015 [PhD thesis].
[56] V. Tvergaard, A. Needleman, K.K. Lo, Flow localization in the plane strain tensile test, J. Mech. Phys. Solids 29 (1981) 115–142, https://doi.org/10.1016/0022-5096(81)90019-3.
[57] A. Needleman, V. Tvergaard, An analysis of ductile rupture in notched bars, J. Mech. Phys. Solids 32 (1984) 461–490, https://doi.org/10.1016/0022-5096(84)90031-0.
[58] A. Corigliano, S. Mariani, B. Orsatti, Identification of Gurson–Tvergaard material model parameters via Kalman filtering technique. I. Theory, Int. J. Fract. 104 (2000) 349–373, https://doi.org/10.1023/A:1007602106711.
[59] M. Rashid, Dual phase steels, Annu. Rev. Mater. Sci. 11 (1981) 245–266, https://doi.org/10.1146/annurev.ms.11.080181.001333.
[60] C.C. Tasan, J.P.M. Hoefnagels, M. Diehl, D. Yan, F. Roters, D. Raabe, An overview of dual-phase steels: advances in microstructure-oriented processing and micromechanically guided design, Annu. Rev. Mater. Res. 45 (2015) 391–431, https://doi.org/10.1146/annurev-matsci-070214-021103.
[61] M. Calcagnotto, D. Ponge, E. Demir, D. Raabe, Deformation and fracture mechanisms in fine- and ultrafine-grained ferrite/martensite dual-phase steels and the effect of aging, Acta Mater. 59 (2011) 658–670, https://doi.org/10.1016/j.actamat.2010.10.002.
[62] P. Dastur, C. Slater, T. Moore, C. Davis, Martensite size and morphology influence on strain distribution and micro-damage evolution in dual-phase steels; comparing segregation-neutralised and banded grades, Mater. Des. 246 (2024) 113340, https://doi.org/10.1016/j.matdes.2024.113340.
[63] N.I. Rohaizat, Fracture of automotive high strength steels, The University of Sheffield, Sheffield, 2018 [PhD thesis].
[64] C. Tian, C.F. Kusche, A. Medina, S. Lee, M.A. Wollenweber, R. Pippan, S. Korte-Kerzel, C. Kirchlechner, Understanding the damage initiation and growth mechanisms of two DP800 dual phase grades, Mater. Des. 238 (2024) 112630, https://doi.org/10.1016/j.matdes.2024.112630.